UHASSELT

KNOWLEDGE IN ACTION

Faculteit Wetenschappen

master in materiomics

Masterthesis

An In-Depth Study of the Thermodynamics and Kinetics of the Structural Phase Transition of Hydrothermally Synthesized W/VO2 Microparticles

Elvan Heirman

Scriptie ingediend tot het behalen van de graad van master in materiomics

PROMOTOR :

Prof. dr. Marlies VAN BAEL

Prof. dr. Pascal BUSKENS

UHASSELT

KNOWLEDGE IN ACTION

www.uhasselt.be

Universiteit Hasselt

Campus Hasselt:

Martelarenlaan 42 | 3500 Hasselt

Campus Diepenbeek:

Agoralaan Gebouw D | 3590 Diepenbeek

2024

2025

UHASSELT

KNOWLEDGE IN ACTION

Faculteit Wetenschappen

master in materiomics

Masterthesis

An In-Depth Study of the Thermodynamics and Kinetics of the Structural Phase Transition of Hydrothermally Synthesized W/VO2 Microparticles

Elvan Heirman

Scriptie ingediend tot het behalen van de graad van master in materiomics

PROMOTOR :

Prof. dr. Marlies VAN BAEL

Prof. dr. Pascal BUSKENS

An In-Depth Study of the Thermodynamics and Kinetics of the Structural Phase Transition of Hydrothermally Synthesized W/VO_2 Microparticles

Elvan Heirman[1,], Stijn Cosemans[1,2], Luc Leufkens[3,4], Marcel A. Verheijen[5,6], Ken Elen[1,2,7], Daniel Mann[1,3,4], Marlies K. Van Bael[1,2,7], Pascal Buskens[1,3,4]*

[1] Design and Synthesis of Inorganic Materials (DESINe), Institute for Materials Research, Hasselt University, Agoralaan Building D, 3590, Diepenbeek, Belgium

[2] IMEC vzw, IMOMEC Associated Laboratory, Wetenschapspark 1, 3590, Diepenbeek, Belgium

[3] The Netherlands Organisation for Applied Scientific Research (TNO), High Tech Campus 25, 5656 AE, Eindhoven, the Netherlands

[4] Brightlands Materials Center, Urmonderbaan 22, 6167 RD, Geleen, the Netherlands

[5] Department of Applied Physics, Eindhoven University of Technology, 5600 MB, Eindhoven, the Netherlands

[6] Eurofins Materials Science, High Tech Campus 11, 5656 AE, Eindhoven, the Netherlands

[7] EnergyVille, Thor Park 8320, 3600, Genk, Belgium

E-mail address: elvan.heirman@student.uhasselt.be

Keywords: tungsten (W) doped vanadium dioxide (VO_2), structural phase transition (SPT), nucleation, isoconversional kinetic analysis, activation energy, thermochromic, hydrothermal synthesis

Abstract: This study investigates the incorporation of tungsten as a dopant in vanadium dioxide through hydrothermal synthesis using vanadyl oxalate and ammonium metatungstate hydrate. The effects of static and rotating reaction setups are examined on particle size and switching performance of the W-doped VO_2 particles. SEM analyses are performed to investigate the particle size and morphology, and DSC results reveal a broad transition peak for both setups, indicating the presence of multiple W-doped VO_2 species with varying tungsten concentrations. Further investigation focuses on tungsten concentrations ranging from 0.0 to 2.0 at.% W. Samples with 0.5 to 1.5 at.% W display a decrease in peak temperature, whereas those with higher concentrations unexpectedly show elevated peak temperature values. Anomalies in transition temperatures highlight the challenges of achieving uniform doping, with TEM-EDX confirming non-uniform tungsten incorporation. Additionally, a detailed thermokinetic analysis of the phase transition of W-doped VO_2 is performed, revealing a kinetic asymmetry, as the activation energy decreases more intensively for the transition of VO_2 (M) to VO_2 (R) than for the opposite transition. Overall, this work underscores the complexities of W-doping in VO_2 and sets the stage for future optimization of the hydrothermal synthesis process to enhance reproducibility and performance of W-doped VO_2 particles.

Abstract (Nederlands): Deze studie onderzoekt de incorporatie van wolfraam als doteringsmiddel in vanadiumdioxide door middel van hydrothermale synthese met vanadyloxalaat en ammonium meta-wolframaat-hydraat. De effecten van statische en roterende reactieopstellingen op de deeltjesgrootte en schakelefficiëntie van de W-gedoteerde VO_2 deeltjes worden onderzocht. SEM analyses worden uitgevoerd om de deeltjesmorfologie te onderzoeken en DSC resultaten onthullen een brede overgangspiek voor beide opstellingen, wat duidt op de aanwezigheid van meerdere W-gedoteerde VO_2-soorten met variërende wolfraamconcentraties. Verder onderzoek richt zich op wolfraamconcentraties variërend van 0,0 tot 2,0 at.% W. Stalen met 0,5 tot 1,5 at.% W vertonen een afname in piektemperatuur, terwijl stalen met hogere concentraties onverwacht verhoogde waarden voor de piektemperatuur laten zien. Anomalieën in overgangstemperaturen benadrukken de uitdagingen van het bereiken van uniforme dotering, waarbij TEM-EDX niet-uniforme wolfraam incorporatie bevestigt. Bijkomend wordt een gedetailleerde thermokinetiek analyse van de faseovergang van W-gedoteerd VO_2 uitgevoerd, waarbij een kinetische asymmetrie wordt vastgesteld, waarbij de activeringsenergie sterker afneemt voor de overgang van VO_2 (M) naar VO_2 (R) dan voor de tegenovergestelde overgang. Over het geheel genomen onderstreept dit werk de complexiteit van W-dotering in VO_2 en legt het de basis voor toekomstige optimalisatie van het hydrothermale syntheseproces om de reproduceerbaarheid en prestaties van W-gedoteerde VO_2-deeltjes te verbeteren.

1 Introduction

1.1 Thermochromic vanadium dioxide (VO_2)

Buildings account for over 40% of global energy consumption, making their energy efficiency crucial for addressing climate change.[1] A significant portion of this energy - 44% - is used by heating and cooling systems in commercial buildings, which also contribute to more than one-third of global anthropogenic carbon dioxide emissions.[2,3] To tackle these challenges and meet increasing energy demands, enhancing energy efficiency in buildings has become essential. Considering, windows being the major cause of their energy inefficiency, as they are responsible for 45% of total energy loss, improving their performance is crucial.[4] Thermochromic windows have sparked the interest of scientists due to its ability to adapt its optical and electrical properties, and therefore its solar heat gain, based on temperature. This self-regulating property can contribute to the reduction of energy consumption for heating and air conditioning in buildings.[5,6]

Vanadium dioxide (VO_2) is one of the species of interest because of its thermochromic properties.[5] At a critical switching temperature (T_0) of approximately 68 °C, VO_2 encounters a reversible structural phase transition (SPT) from monoclinic VO_2 (M) (**Figure 1b**) to tetragonal rutile VO_2 (R) (**Figure 1a**). This SPT can be considered as a continuous process with consecutive intermediate structures between VO_2 (M) and VO_2 (R). During this transition from VO_2 (M) to VO_2 (R) the vanadium ions positioned on the zigzag chain move resulting in a linear chain ($\delta = 0$); starting from a chain with two different V-V distances, i.e. 3.19 Å and 2.60 Å, present to a chain where the vanadium ions are equidistant with a V-V distance of 2.85 Å. Correspondingly, a partial octahedron at lower temperatures transitions to a normal octahedron at higher temperatures, resulting in a symmetry increase and a unit cell volume reduction by a factor of two.[3,7,8]

This SPT is accompanied by a first-order metal-insulator transition (MIT), as firstly reported by Morin *et al.* in 1959. VO_2 (M) is a semiconductor characterized by its ability to transmit infrared (IR) light effectively when it's maintained below its critical temperature, rendering it IR-transparent. Whereas, VO_2 (R) functions as an electrical conductor that blocks IR light at elevated temperatures, making it IR-blocking. This distinctive property of VO_2, which enables contrasting transmission behaviors without the necessity for active control systems, makes it a

crucial area of study in the development of smart windows for improved thermal regulation in buildings. The deployment of energy-efficient smart windows utilizing VO_2 has the potential to significantly reduce energy consumption related to temperature control, thereby making a meaningful impact on global energy efficiency.[5,6,9]

In 1971, Goodenough *et al.*[10] stated that the octahedral coordination of vanadium ions with oxygen ions, in VO_2 (R) (**Figure 1c**), causes the V 3d-orbital to split into e_g- and t_{2g}-symmetry states. In addition, the t_{2g} states are further split into two d_π orbitals, comprised of a π bond and a π^* anti-bond, and one d// orbital. The metallic characteristics of IR-blocking VO_2 (R) arise from the partial energetic overlap between the π^* and d// bonds at the Fermi level. In VO_2 (M) (**Figure 1d**), the lattice distortion results in the elevation of the energy level of the π^* bond above the Fermi level, enhancing the π overlap between the V^{4+} and O^{2-} orbitals. The dimerization of the V-V pairs induces the splitting of the d// bonds into d//-bonding and anti-bonding components, resulting in a bandgap of 0.7 eV between the π^* and d//-bonding levels, giving rise to the semiconductive properties in IR-transparent VO_2 (M).[3,7,8,10,11]

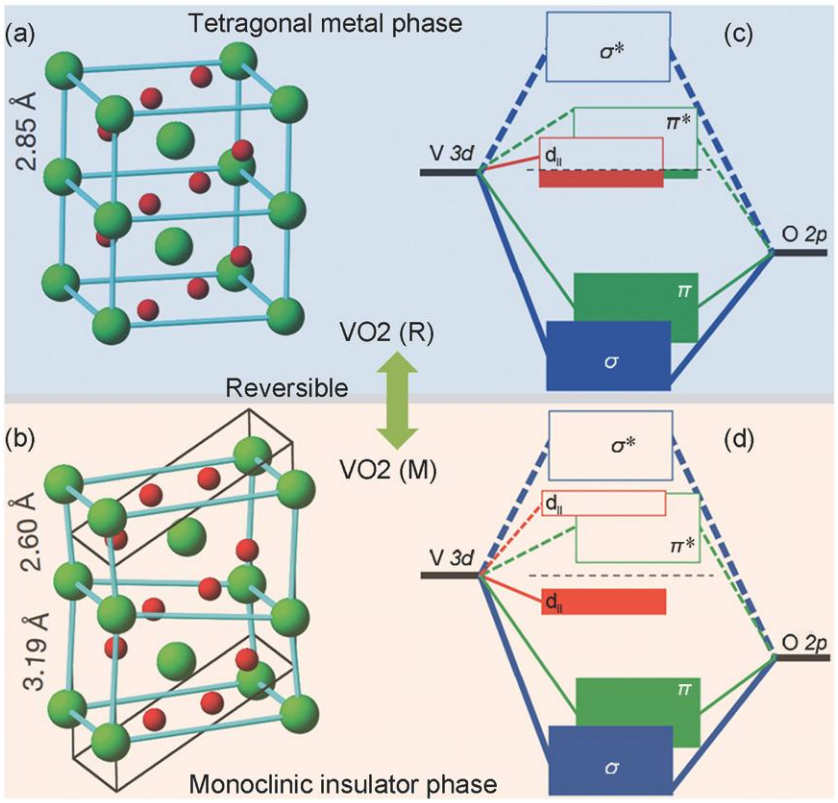

Figure 1. Schematic of crystal structure of VO_2 in the a) metallic and b) insulating states. V ions: larger and green balls; O ions: smaller and red balls. Schematic of electronic band structure of c) VO_2 (R) and d) VO_2 (M) based on crystal-field model.[3]

1.2 Optimalization of VO_2 for its practical implementation

For practical implementation of VO_2 in thermochromic smart windows the following three parameters need to be altered and improved: the critical switching temperature (T_0), the luminous transmittance (T_{lum}), the solar modulation (ΔT_{sol}).

1.2.1 Optimalization of the critical switching temperature T_0

First, for optimum energy savings in thermochromic windows, the T_0 of VO_2 must be reduced from its intrinsic value of 68 °C to a range of 15-25 °C. This adjustment can be realized by introducing intrinsic point defects, such as oxygen vacancies, incorporating metal ion dopants, or applying strain within the crystal structure. Among these approaches, elemental doping is an effective strategy. Doping can enhance the electrical and optical properties of VO_2 due to the introduction of specific metal ions in the crystal lattice of VO_2. As a result the energy barrier of the phase transition is altered, hereby lowering the T_0. However, the exact physical mechanism behind this phenomenon is still unclear and has resulted in an ongoing debate among experts. Some argue that the phase transition is entirely driven by electron-electron interactions, i.e. the Mott transition, while others believe it is mainly due to structural distortions, i.e. the Peierls transition.[3,7,8,12]

As the electronic phase transition of VO_2 is associated to a typical Mott phase transition, an increase in the charge carrier concentration results in a decrease of the T_0. Doping can increase the number of available charge carriers within the VO_2 lattice, thereby increasing the probability of electronic interactions, as the electron density in the conduction band of VO_2 increases. As a result, the band structure is affected and the energy barrier across the phase transition is lowered, leading to a decrease in T_0. If the structural phase transition of VO_2 is associated with a typical Peierls phase transition, the introduction of distortion into the atomic structure promotes the SPT by lowering the energy barrier and thereby decreasing the critical temperature T_0. Structural distortions along the V-V chains are effective in reducing the energy needed for the SPT as the key difference between the metallic and the insulating phase lies in the V-V bond lengths. In VO_2 (R), these distances remain constant, while they vary in VO_2 (M). Regardless of the theory, it is generally accepted that the effectiveness of doping in modifying T_0 is contingent upon the charge and size of the ions introduced, as they play a critical role in affecting the carrier density within the conduction band of VO_2 and the crystal structure.[3,7,8,12]

Among potential dopants, tungsten (W^{6+}) is particularly effective in reducing the transition temperature of VO_2 to room temperature. By substituting vanadium sites with the high-valence W^{6+}, electrons can be injected into the V_{3d} valence band of VO_2, hereby improving the phase transition. Furthermore, the local structure around W dopants was identified as an expanded intrinsically symmetric tetragonal structure, which produces internal stresses, driving the detwisting of the nearby asymmetric monoclinic VO_2 lattice towards the rutile phase. It was stated that this structure acts as the structure-guided domain to facilitate the MIT in VO_2. As a result, tungsten doping decreases T_0 by approximately 22 °C per at.% W, with two at.% W reducing the transition temperature to 15 – 20 °C.[5,6,8,12,13]

1.2.2 Optimalization of the luminous transmittance T_{lum} and the solar modulation ΔT_{sol}

Furthermore, implementation of VO_2 particles in coatings for smart windows requires both a high luminous transmittance (T_{lum}) (≥ 60%) and a high modulation of solar energy (ΔT_{sol}) (≥ 10%). T_{lum} corresponds with the quantity of visible light (380 – 780 nm) that passes through a transparent material and ΔT_{sol} is defined as the difference between the solar transmission (300 – 2500 nm) of VO_2 (M) and VO_2 (R).[11] Since both these parameters influence the efficiency of thermochromic smart windows, a significant amount of research has been carried out to optimize their inherent trade-off, as an increase in T_{lum} generally results in a decrease of ΔT_{sol} and vice versa. For instance, Granqvist *et al.*[5] introduced the concept of nanothermochromic coatings and films to improve both these parameters. To achieve this increase in both T_{lum} and ΔT_{sol} the nanoparticles should have a particle size well below the wavelength of visible light (≤ 100 nm) to avoid scattering of visible light, the particles need to have a high purity and crystallinity to ensure good switching performance, and random dispersion in the film or coating is required. In parallel, Li *et al.* investigated the optical properties of VO_2 nanoparticle films through simulations and computational methods, resulting in a similar conclusion; while improving ΔT_{sol} a notable increase in T_{lum} could be accomplished by decreasing the size of VO_2 nanoparticles to dimensions smaller than the wavelength of visible light.[5] Furthermore, previous studies highlight the significance of nanoparticles smaller than 100 nm, as they exhibit a transmittance minimum around 1200 nm due to localized surface plasmon resonance (LSPR) of metallic VO_2 (R). This feature is vital for reducing near-infrared transmittance in the metallic state, thereby enhancing solar modulation, and minimizing light scattering to maintain film transparency.[5]

1.3 Production techniques to synthesize VO_2 (M) nanoparticles

Synthesizing pure stoichiometric monoclinic VO_2 (M) crystals presents several challenges due to the existence of over 20 stable vanadium oxide phases. This results in a complex V-O phase diagram comprising a diverse range of compounds and crystal structures. One significant issue is that VO_2 can easily oxidize to vanadium pentoxide (V_2O_5) when exposed to oxygen at elevated temperatures. Additionally, VO_2 exhibits multiple polymorphs with varying crystal structures, space groups and unit cell parameters, influenced by the specific arrangement of vanadium and oxygen ions. Notable polymorphs include VO_2 (M1) ($P\,2_1/c$), VO_2 (M2) ($C\,2/m$), VO_2 (R) ($P\,4_2/mnm$), VO_2 (A) ($P\,4_2/nmc$), VO_2 (B) ($C\,2/m$), VO_2 (C) ($I\,4/mmm$), VO_2 (D) ($P\,2/c$), and VO_2 (P) (*Pbnm*). Consequently, achieving phase purity and controlling the resulting phase during the synthesis process is crucial, particularly for VO_2 (M) and VO_2 (R), which are essential for exhibiting thermochromic properties suitable for smart window applications. In the context of this thesis, the stable phase VO_2 (M1) will be referred to simply as VO_2 (M).[3,5,14]

The fabrication of vanadium dioxide (VO_2) in its monoclinic (M) phase can be accomplished by different synthesis methods. Both top-down and bottom-up nanofabrication techniques have been explored. The top-down approach involves breaking down bulk materials into nanoscale structures, typically through bead milling. This method is scalable and adaptable for both batch and continuous operations; however, it faces challenges such as high energy consumption, increased costs, and potential loss of crystallinity. In contrast, bottom-up techniques creates nanoparticles from atoms or molecules as starting material, allowing for better control over their morphology and composition. In case of VO_2 (M), this implies hydrothermal synthesis, which involves a heterogeneous reaction in an aqueous solvent under high pressure and temperature conditions in a closed system, such as an autoclave. These reaction conditions allow materials which are relatively insoluble to dissolve and recrystallize. The hydrothermal synthesis of VO_2 has many advantages, such as good crystallinity, wide application range, simple experimental process, and high yield. However, it also has some limitations like high-pressure risks and dependence on toxic reducing agents, such as the highly flammable, reactive, and toxic hydrazine, which is raising significant health and safety concerns when scaling up for industrial applications. In selected studies, the hydrothermal synthesis of VO_2 (M) was employed without the use of the toxic hydrazine as reducing agent.[3,5,6,8,11,14–16]

1.4 Research objectives

In this manuscript, the incorporation of tungsten as dopant in VO_2 during hydrothermal synthesis, starting from vanadyl oxalate and ammonium metatungstate hydrate as metallo-organic precursors, is investigated.[6] First the impact of rotation on the particle size of W-doped VO_2, and its influence on the switching performance is studied. Hereafter, the concentration of tungsten relative to the amount of vanadium is being varied, while the reaction time and environmental conditions are held constant, to investigate the effect of doping on the switching performance. Lastly, the impact of incorporated W^{6+} on the switching performance of W/VO_2 particles, i.e. the thermodynamics and kinetics, is investigated.

2 Experimental

2.1 Experimental procedure to synthesize W-doped VO_2 nanoparticles

The synthesis of the hereafter described tungsten-doped VO_2 powder was based on the procedure established by Timmers *et al.*[6] in 2024. Some deviations or additional steps from this procedure were introduced to conduct the described study.

Vanadyl(IV) oxalate solution was prepared at room temperature by the addition of vanadium(V) oxide (V_2O_5; 0.202 g; 1.11 mmol; 1.00 equiv., 99.6% min, Thermo Scientific) and oxalic acid ($C_2H_2O_4$; 0.200 g; 2.22 mmol; 2.00 equiv.; 98%; Sigma-Aldrich) in Milli-Q water (20 ml). The solution was stirred for 1 h at room temperature using a magnetic stirring bar, to obtain a homogeneous dissolution. Next, for the synthesis of the tungsten comprising precursor, ammonium metatungstate hydrate ($(NH_4)_6H_2W_{12}O_{40}\cdot H_2O$; 99.99%; Sigma-Aldrich) was added to this vanadyl(IV) oxalate solution. The amount of $(NH_4)_6H_2W_{12}O_{40}\cdot H_2O$ added, depended on the preferred dopant concentration (**Table S1.1**).

Subsequently, the tungsten-containing vanadyl(IV) oxalate solution was transferred to a Teflon-lined autoclave (Parr 4744 45 ml General Purpose Vessel; Parr CUF W/Cover 45ml 4744 PTFE; Parr Blow-off Disc 4744/49 INC; Parr Corrosion Disc). The autoclave was either placed vertically static or horizontally rotating, using a rotational device (Broilfire ST-40S), in a convection oven (Memmert Universal oven UF30) (**Figure S1.1**) at 230 °C and kept for 72 h. After the product was air-cooled to room-temperature, the obtained dispersion was centrifuged and the resulting black reaction product was collected. Subsequently, the reaction powder was purified by washing and centrifugation (Eppendorf Centrifuge 5804 R) in ethanol (C_2O_5OH; 15ml; 99.8%; Fisher Chemical) for three times 11 minutes on 11000 rpm. Hereafter, the product was dried overnight in a vacuum oven (Thermo Fischer Scientific VACUtherm vacuum oven VT6025) at 50 °C and at a reduced pressure of 50 mbar.

2.2 Characterization techniques

2.2.1 Differential Scanning Calorimetry (DSC)

DSC analyses were carried out on the dried powder products in air using a Discovery DSC (TA Instruments). For analysis, 20 mg of W-doped VO_2 powder were placed in aluminum pans (TA Instruments, T_{zero} aluminum pan with T_{zero} lid), as it is reported by Calvi *et al.*[17] that both lower and higher masses lead to unwanted effects. At lower masses, the weighing error causes substantial deviations in the obtained results, while at higher masses, the high thermal mass causes a delay and distortion in time of the heat flow signal due to heat storage within the sample, leading to an undesired broadening of the DSC signal over a broad temperature range.[17] To investigate the influence of the amount of W present, all samples were subjected to three cycles of heating and cooling at a rate of 20 °C·min^{-1}. For thermokinetic analysis, all samples were subjected to the following five heating and cooling rates between −60 °C and 120 °C: 2.5, 5, 10, 15, and 20 °C·min^{-1}. The collected data were analyze with TRIOS software v5.1 and processed in accordance with the Friedman's isoconversional method (see section 3.3).[6,17–19]

The peak temperature has been defined as the temperature corresponding to the minimum heat flow in the heat up cycle. The switching enthalpy (ΔH_{switch}) has been defined as the integration of the heat flow curve in the temperature range identical to this one of the running integral (see section 3.3), as it corresponds to the energy needed for the phase transition of 1 g of material. The hysteresis has been defined as the difference between the peak temperature of the heating and the peak temperature of the cooling curve. The peak width, corresponding to the hysteresis gradient, has been defined as the difference between temperature at 0% and 100% conversion.[6]

For thermokinetic analysis (see section 3.3), the running integral of the DSC peak is processed to obtain a conversion-temperature (α-T) profile and a conversion-time (α-time) profile. From the first plot, $T_{\alpha=0.50}$ is extracted, as it corresponds to the temperature at 50% conversion (α = 0.50). The second plot allows to determine the conversion rate at 50% conversion, by using the first derivative of the conversion-time plot between 40% and 60% conversion. Hereafter, both values are applied to produce a Friedman plot, from which the first derivative is defined as the activation energy of the phase transition.[17]

The temperature range utilized for calculating the switching enthalpy and the running integral of the DSC curve was established from the 20 °C·min^{-1} curve. The end point of this range corresponds to the temperature at which the DSC curve returns to its baseline following the phase transition. The starting point of the range is determined by calculating the temperature difference between the peak temperature and the end point of the range. This temperature difference is then subtracted from the peak temperature to find the initial value. However, if a peak appears at a lower temperature, this temperature difference is subtracted from the temperature corresponding to the maximum value of that peak, instead of the peak temperature, to determine the initial value.

2.2.2 X-Ray Diffraction (XRD)

XRD analysis was performed to investigate the crystalline components of the W/VO_2 particulate materials. 100 mg of the powder was added to the sample holder of the Bruker D2 Phaser machine equipped with a Lynxeye (1D mode) detector.[6,19] The DIFFRAC.EVA program was used to identify the signals.[6,18]

2.2.3 Scanning Electron Microscopy (SEM)

The TENEO Scanning Electron Microscope (SEM) was used for obtaining electron images of the hydrothermally synthesized W-doped VO_2 crystals at either 20.000 kV or 10.000 kV and at 6.3 pA. A drop of the sample dispersion was placed onto a metal substrate that was attached to an aluminum mounting pin. The sample was dried for one minute, after which any excess liquid was removed using a paper towel. Surface topography images were captured using the Everhart-Thornley Detector (ETD).[6,18,19]

2.2.4 Transmission Electron Microscopy – Energy Dispersive X-Ray Spectroscopy (TEM-EDX)

TEM studies were performed at Eurofins EAG Materials Science using a KEOL ARM 200F probe corrected Transmission Electron Microscope operated at 200 kV. Imaging of the particles was performed using complementary Bright Field (BF)-scanning TEM (STEM) and High Angle Annular Dark Field (HAADF)-scanning TEM (STEM). The samples were prepared by sonification in IPA, whereafter 4 µl was placed on a holey carbon film and dried under ambient conditions. From BF-STEM an image can be obtained showing contrast between masses and diffraction. As a result, for a sample consisting of randomly oriented crystals each crystal will have its own grey-level. This enables the distinguishment between different materials as well as image individual crystals and crystal defects. HAADF-STEM images were obtained by the HAADF detector, which uses the electrons scattered over large angles for imaging. The HAADF detector is therefore mass sensitive, leading to higher brightness in the image for samples with a larger concentration present or heavier atoms or both. Energy Dispersive X-Ray Spectroscopy (EDX) spectra were recorded by a 100 mm² Centurio SDD EDX detector. The W content from EDX analysis was calculated as at. % between V and W in the crystals, excluding the O content. The uncertainty of the dimensional TEM measurements is better than ± 5%, providing an estimated level of confidence of 95% using a coverage factor k = 2 for well-defined features > 3 nm.[6]

3 Results and Discussion

3.1 The influence of static or rotating reaction conditions during the hydrothermal synthesis

The effect of mixing during hydrothermal synthesis on the uniformity of VO_2 particles was investigated, employing two different setups. The first was a static setup, where the reactors were placed upright in a convection oven without any stirring or movement during the reaction. In the second system (**Figure S1.1**), a rotating setup was fabricated by incorporating a system into the convection oven, allowing the autoclaves to rotate horizontally at a constant speed of 2.5 rpm. The samples were prepared according to the method described in section 2.1 and both were doped with 2.0 at.% W^{6+}.

DSC analysis (**Figure 2a, Table 1**) allowed to determine the phase transition temperature and the enthalpy of the prepared samples. Overall, the phase transition signals in the DSC measurements for all VO_2 particles from rotation experiments are less broad than for particles from static experiments, despite still showing shoulder peaks. The reduction in peak width is likely caused by a reduction in particle size distribution upon rotation. The fact that multiple peaks at different temperatures together form the switching signals indicates the presence of multiple W-doped VO_2 species, indicating the non-uniform tungsten distribution in both the rotating and statically produced particles.

This observation is further supported by the overlap in the temperature ranges for the transitions from VO_2 (M) to VO_2 (R) and *vice versa*. According to equation (4) and (5) (see section 3.3), thermodynamic principles indicate that no overlap should occur for a single pure species. This suggests that, under both rotational and static conditions, multiple VO_2 (M) species are produced, each with a different concentration of W-dopant. Additionally, a higher peak temperature is observed for product mixtures from experiments conducted with rotation compared to products from experiments conducted without rotation. This difference is attributed to increased uniformity and reduced peak width in the rotational setup. In addition, both experimental setups yielded similar enthalpy values, approximately 20 J/g for cooling and 15 J/g for heating. From a thermodynamic theoretical perspective, the enthalpy of both the phase transition from monoclinic to rutile as well as the phase transition of VO_2 (R) to VO_2 (M) should be the same, as enthalpy is a material constant. However, this discrepancy arises from

the complexity of integration methods used and the challenges encountered when reaching and exceeding the cooling limit of DSC apparatus.

XRD analysis (**Figure 2b**) was performed to investigate the crystal structure and identify the formed vanadium oxide polymorphs. Samples prepared under static conditions typically display less intense signals in their diffractograms compared to those from samples prepared under rotating conditions. In the diffractogram of the static samples, a broad hump appears between 20° and 35°, indicating the presence of amorphous material. This hump is absent in the diffractogram of the rotating samples, highlighting that rotation leads to higher crystallinity. Moreover, both synthesis conditions result in the formation of VO_2 (M) and VO_2 (A) polymorphs, with a greater amount of VO_2 (M) found in samples produced under rotational conditions than in those prepared statically. The XRD results (**Figure 2b**) align with the observations from DSC analysis (**Figure 2a, Table 1**), which shows that samples synthesized under rotational conditions exhibit narrower DSC peaks during the structural phase transition between VO_2 (M) and VO_2 (R) and vice versa.

SEM analysis (**Figure 2c,d**) allowed the investigation of the size and shape of the VO_2 particles. It shows a difference of approximately 35 percent in arm length and width between the average size of the asterisk-shaped VO_2 (M) crystals from rotational experiments, with an arm length of 5.67 ± 3.48 µm and a width of 0.66 ± 0.18 µm (**Figure S2.1**), and static experiments, with an arm length of 8.80 ± 4.33 µm and a width of 0.99 ± 0.56 µm (**Figure S2.2**). A similar trend can be observed, with a difference of approximately 40 percent in length and 80 percent in width, for crystal bars produced under rotating and static conditions, which have a length of 4.77 ± 1.61 µm and 8.33 ± 1.90 µm, and a width of 0.41 ± 0.32 µm and 1.86 ± 1.09 µm, respectively (**Figure S2.1, S2.2**). On size distribution level, a distinguishment can be made between both setups as the particles produced under rotational conditions have a smaller standard deviation in both length and width than those produced under static conditions. This observation aligns with earlier research of Timmers *et al.*[6], by indicating that the use of rotational mixing significantly increases the uniformity of the synthesized VO_2 particles.

Table 1. Enthalpy (ΔH_{switch}), peak temperature, temperature at 50% conversion ($T_{\alpha=0.50}$), and hysteresis of hydrothermally synthesized VO_2 particles with the addition of 2.0 at.% W obtained under rotating or static conditions after 72h in an autoclave at 230 °C.

	Temp rate [°C/min]	Enthalpy (ΔH_{switch}) [J/g]		Peak temp [°C]		$T_{\alpha=0.50}$ [°C]		Hysteresis [°C]
		Cooling	Heating	Cooling	Heating	Cooling	Heating	
2.0 at.% W (rotating)	2.5	19.320	14.604	35.89	43.59	30.57	44.24	7.70
	5	19.068	14.766	34.54	44.50	29.83	44.61	9.96
	10	19.112	14.800	33.56	45.02	29.32	44.60	11.46
	15	18.929	14.829	33.78	45.35	29.03	44.69	11.57
	20	18.728	14.939	33.31	45.41	28.80	45.07	12.10
2.0 at.% W (static)	2.5	20.961	14.904	25.18	31.42	22.09	35.75	6.24
	5	20.862	15.475	24.74	31.86	20.42	36.27	7.12
	10	20.666	15.665	23.07	32.76	19.53	36.37	9.69
	15	20.574	15.444	23.46	33.23	20.10	36.44	9.77
	20	22.013	15.326	23.82	32.50	20.75	36.60	8.68

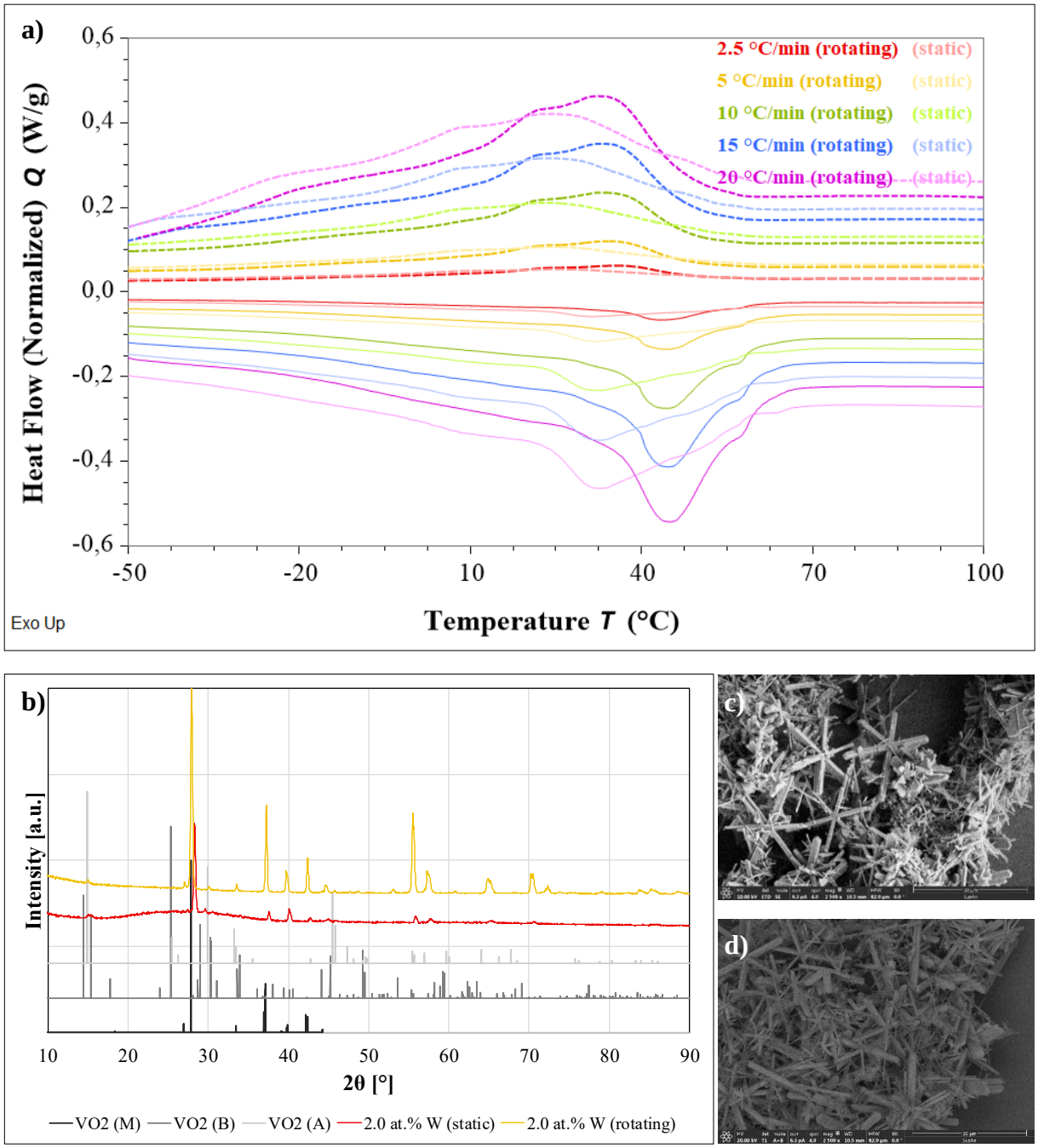

Figure 2. a) DSC heating (solid) and cooling (dotted) graphs of hydrothermally synthesized VO_2 particles with the addition of 2.0 at.% W obtained under rotating (darker color) or static (lighter color) conditions after 72h in an autoclave at 230 °C obtained at different heating rates, ranging °C·min^{-1} from 2.5 till 20 °C·min^{-1}, b) XRD diffractogram of these samples, with reference spectra for VO_2 (M) (PDF 72-0514), VO_2 (B) (PDF 31-1438), and VO_2 (A) (PDF 42-0876), c) SEM image obtained for the sample under rotating conditions, d) SEM image obtained for the sample under static conditions.

3.2 The influence of different concentrations of W^{6+} dopant

After concluding the improvement in uniformity of the obtained VO_2 particles by rotating the autoclaves during hydrothermal synthesis, the incorporation of tungsten (W) into the VO_2 lattice was investigated. The hydrothermal synthesis, as described in section 2.2, was carried out under rotating conditions while varying the W-dopant concentration from 0 at.% to 2.0 at.% (**Table S1.1**). However, it is important to approach the following results and interpretations with caution, as not all experiments could be replicated due to time constraints. Additionally, some of the reproduction experiments did not yield results consistent with those of previous experiments conducted during this research.

DSC analysis (**Figure 3**, **Table 2**) was conducted at a heating rate of 20 °C·min^{-1} to study the phase transition from VO_2 (M) to VO_2 (R) and from VO_2 (R) to VO_2 (M). The DSC curve for the product synthesized without the W-dopant did not display the characteristic phase transition peak for VO_2 (M) around 68 °C. Instead, a phase transition was observed around 170 °C, with a ΔH_{switch} of approximately 7.0 J·g^{-1}, distinctive for VO_2 (A) (**Figure S3.1**). For the W-doped samples, with a degree of doping between 0.5 at.% and 2.0 at.% W, it was expected that the critical temperature (T_0) would decrease with increasing dopant concentration, with previous research indicating that the critical temperature of VO_2 decreases by 22 °C for each at.% of W added.[5] The DSC results for the samples prepared via hydrothermal synthesis, as detailed in section 2.2, exhibit a partial alignment with this expected trend. Specifically, during the transition from monoclinic to rutile phase, samples containing 0.5 to 1.5 at.% W demonstrate a decrease in peak temperature, which is consistent with expectations. Conversely, the samples with 1.7 and 2.0 at.% W show transition temperatures that are similar to those of the sample with 1.3 at.% W. Notably, for the transition from VO_2 (R) to VO_2 (M), this anticipated trend is completely absent.

The critical transition temperature for pure VO_2 (M) is 68 °C for the transition from monoclinic to rutile.[5] The observed transition temperature of 54.60 °C for the sample prepared with the addition of 0.5 at.% W aligns well with the theoretically expected value of 57 °C (**Figure 3**, **Table 2**). Similarly, the sample with 1.3 at.% W shows a reasonable agreement with the expected transition temperature of 39.4 °C, as it has a measured peak temperature of 45.80 °C. However, the transition temperatures for the samples with 1.5 at.% and 1.7 at.% W, which are 25.49 °C and 45.13 °C, respectively, differ significantly from their theoretical values of 35.0

°C and 30.6 °C. This discrepancy increases further for the sample containing 2.0 at.% W, where the observed peak temperature is 47.59 °C, which is more than 20 °C higher than the expected value of 24.0 °C. Thus, as more W was added to the vanadyl(IV) oxalate solution, the deviation from the theoretically expected value for the peak temperature increased. These results suggest an inhomogeneous distribution and incomplete incorporation of tungsten within the samples.

This uneven distribution of W also gave rise to the formation of multiple VO_2 species within a single sample, each with different dopant concentrations. For instance, the particles with 0.5 at.% W exhibited a broad DSC peak ranging over 56 °C, from −5 °C to 51 °C, for the transition of VO_2 (R) to VO_2 (M), and a DSC peak with a width of 38 °C, spanning from 33 °C to 71 °C, for the transition of VO_2 (M) to VO_2 (R) (**Figure 3**, **Table 2**). The sample with 1.5 at.% W also displayed broad exothermic and endothermic peaks, ranging over 40 °C and 60°C, respectively. The peak widths for the 1.3 at.% and 1.7 at.% W-doped samples were 48 °C and 44 °C for the VO_2 (R) to VO_2 (M) transition, and 58 °C and 42 °C for the VO_2 (M) to VO_2 (R) transition, respectively. Additionally, both these samples exhibited a shoulder peak in the cooling curve, indicating the presence of multiple VO_2 species. The appearance of this shoulder peak at a temperature lower than the maximum signal, referred to as peak fronting, suggests the presence of samples with a higher degree of doping than 1.3 at.% and 1.7 at.%, or the introduction of other defects, such as oxygen vacancies, into the VO_2 (M) crystal lattice. This observation of small fractions of highly doped crystals is further supported by the critical switching temperature being more than 2 °C lower than the anticipated peak temperature of the main peak. The DSC results for the sample with 2.0 at.% W demonstrated, similar to the previous samples, a broad transition peak of 32 °C, ranging from 27 °C to 59 °C for the transition from rutile to monoclinic, and a broad peak over 42 °C, between 26 °C and 68 °C, for the transition from monoclinic to rutile. These broad signals indicate a greater inhomogeneity in the tungsten distribution among the crystals within one sample, as both higher and lower W concentrations than anticipated are present.

In addition to the critical switching temperature, peak shape and width, the switching enthalpy (ΔH_{switch}), and hysteresis can also be assessed using the DSC results. Reports from various research groups indicated an expected decrease in the switching temperature with increasing dopant concentration, beginning at a ΔH_{switch} of 55 J/g for pure VO_2 (M).[5] However, the observed DSC results did not support this expectation and displayed no clear relationship between enthalpy and dopant concentration. The enthalpy of particles produced with the

addition of 0.5 at.% W show the highest observed enthalpy with 29.7530 J/g for the transition from VO_2 (R) to VO_2 (M) (**Figure 3**, **Table 2**). In contrast, the enthalpy values for the other concentrations are as follows: 1.3 at.% is 18.350 J/g, 1.5 at.% is 13.714 J/g, 1.7 at.% is 17.411 J/g, and 2.0 at.% is 15.802 J/g. Notably, the enthalpy value for particles synthesized with 2.0 at.% W-dopant is approximately 50% lower than the ΔH_{switch} value of 30.4 J/g for VO_2 (M) powders obtained during earlier research of Calvi *et al.*[17], indicating low purity of the VO_2 (M) crystals. Again, it may be noted that the enthalpy of the transition from VO_2 (M) to VO_2 (R) differs from that of rutile to monoclinic. However, this is thermodynamically forbidden since enthalpy is a material constant. This discrepancy probably arises from the complexity of integration methods used and the challenges encountered when reaching and exceeding the cooling limit of DSC apparatus.

Furthermore, the hysteresis observed in the samples varies significantly based on the concentrations of W-dopant used. Notably, the sample with 0.5 at.% W exhibits a substantial hysteresis of 32.22 °C, which may be attributed to its low uniformity (**Figure 3**, **Table 2**). In contrast, the samples containing 1.3 at.% and 1.7 at.% W display a reduced hysteresis of approximately 10 °C. Additionally, the hysteresis levels decrease even more for the samples with 1.5 at.% and 2.0 at.% W, showing values of 7.57 °C and 3.99 °C, respectively. This combination of hysteresis values, along with the broad peaks in the DSC signals, contributes to the overlap in the temperature ranges of the DSC peaks that represent the transitions from VO_2 (M) to VO_2 (R) and from VO_2 (R) back to VO_2 (M) during heating and cooling. This again suggests that multiple VO_2 (M) species are present in the final product mixture due to W doping, likely each with a different dopant concentration. In summary, based on the DSC results, overall, no distinct trends can be observed in the critical transition temperature, peak width, switching enthalpy, or hysteresis of VO_2 (M) particles as W-dopant concentration increases.

To further investigate the different crystal phases that are present in the products synthesized with different amounts of dopant, XRD analysis was performed (**Figure 4a**). For the reaction without the addition of W, the diffractogram confirms the single presence of VO_2 (A). The sample containing 0.5 at.% W exhibits a diffraction pattern comparable to the reference spectrum of VO_2 (M). In contrast, the samples with higher tungsten concentrations of 1.3 at.%, 1.5 at.%, and 1.7 at.% display diffractograms that indicate not only the presence of VO_2 (M) but also the formation of VO_2 (B). In the product obtained by synthesis with 2.0 at.% W, signals

characteristic for VO_2 (M) as well as VO_2 (B) and VO_2 (A) are present, explaining the rather low ΔH_{switch} obtained by DSC.

SEM analyses (**Figure 4b**) of particles produced with 0.5 at.% W, 1.3 at.% W, and 1.7 at.% W display both VO_2 (B) and VO_2 (M) structures. VO_2 (B) is represented by small rod-like structures, while VO_2 (M) is characterized by asterisk-shaped crystals or larger bar-shaped crystals, indicating incomplete asterisks. SEM analyses of particles produced with 0.5 at.% W (**Figure S4.1**) show asterisk-shaped crystals with an average arm length and width of 4.40 ± 2.12 µm and 0.52 ± 0.19 µm, respectively, and larger bar-shaped crystals with a length and width of 8.49 ± 3.24 µm and 1.23 ± 0.27 µm, respectively. The SEM results of VO_2 particles with 1.3 at.% W (**Figure S4.2**) show asterisk-shaped crystals with an arm length and width of 17.66 ± 4.54 µm and 1.32 ± 0.54 µm, respectively, and larger bar-shaped crystals with a length and width of 19.00 ± 6.81 µm and 1.29 ± 0.41 µm, respectively. The SEM results obtained for particles produced with 1.7 at.% W (**Figure S4.3**) are comparable, as they exhibit arm lengths and width of respectively 17.69 ± 6.63 µm and 0.98 ± 0.46 µm for asterisk-shaped crystals, and lengths of 19.29 ± 9.20 µm and widths of 1.15 ± 0.39 µm for bar-shaped crystals. These SEM results support the findings of the earlier described XRD analysis.

To investigate the W distribution within the VO_2 (M) crystals synthesized with 1.5 at.% W, TEM-EDX analysis (**Figure 4c**) was performed. A large spread in W content between the crystals is observed. Crystals with W content between 0.1 and 1.8 at.% are detected, corresponding well with the results obtained from DSC analysis, showing a broad peak width of 26 °C, indicating the presence of multiple VO_2 (M) species with each a different W concentration.

Table 2. Enthalpy (ΔH_{switch}), peak temperature, temperature at 50% conversion ($T_{\alpha=0.50}$), peak width, and hysteresis of hydrothermally synthesized W/VO_2 particles obtained after 72h in a rotating autoclave at 230 °C, with the addition of different amount of W-dopant.

	ΔH_{switch} [J/g]		Peak temp [°C]		$T_{\alpha=0.50}$ [°C]		Peak width [°C]		Hysteresis [°C]
	Cooling	Heating	Cooling	Heating	Cooling	Heating	Cooling	Heating	
0.5 at.%	29.753	27.184	22.38	54.60	23.703	51.223	56.00	38.00	32.22
1.3 at.%	18.354	17.204	35.26	45.80	31.157	44.094	48.00	44.00	10.54
1.5 at.%	13.714	14.851	17.92	25.49	18.260	25.770	40.00	60.00	7.57
1.7 at.%	17.411	13.166	34.97	45.13	32.925	44.740	58.00	42.00	10.16
2.0 at.%	15.802	18.748	43.60	47.59	43.741	49.737	32.00	42.00	3.99

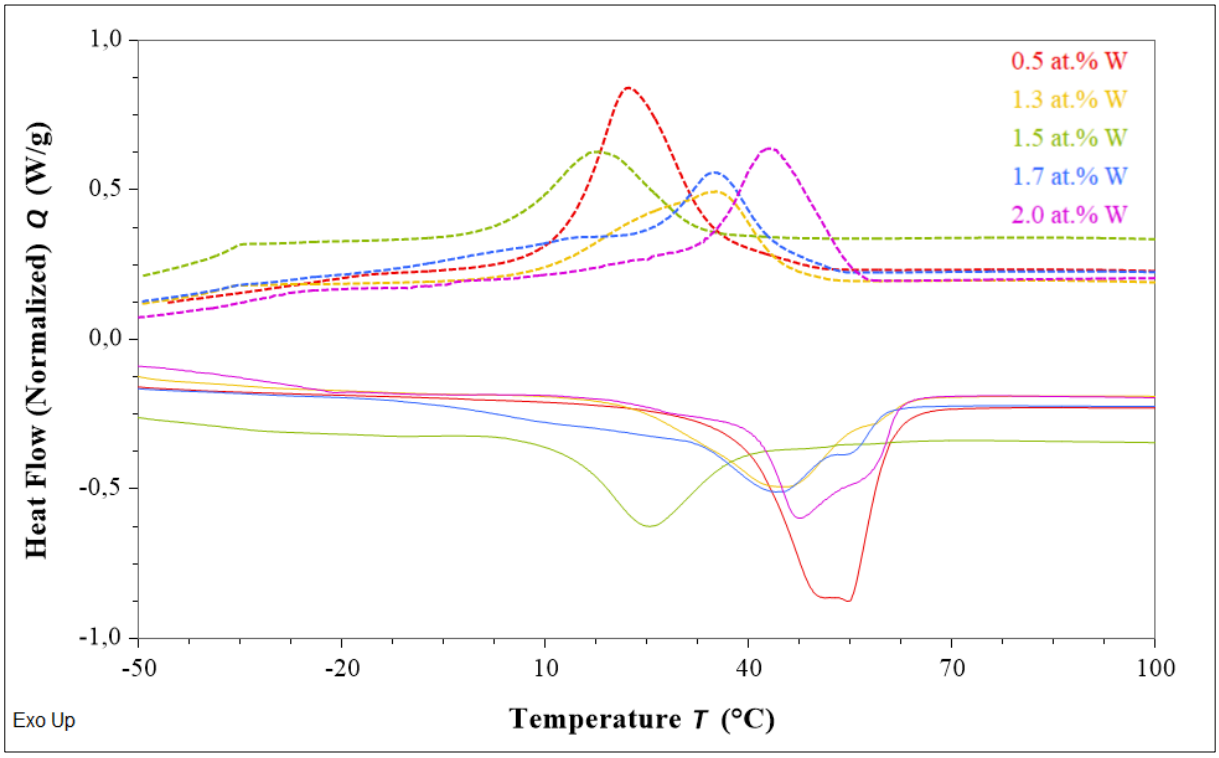

Figure 3. DSC heating (solid) and cooling (dotted) graphs of hydrothermally synthesized W/VO_2 particles obtained at a heating rate of 20 °C·min^{-1} after 72h in a rotating autoclave at 230 °C, with the addition of different amount of W-dopant.

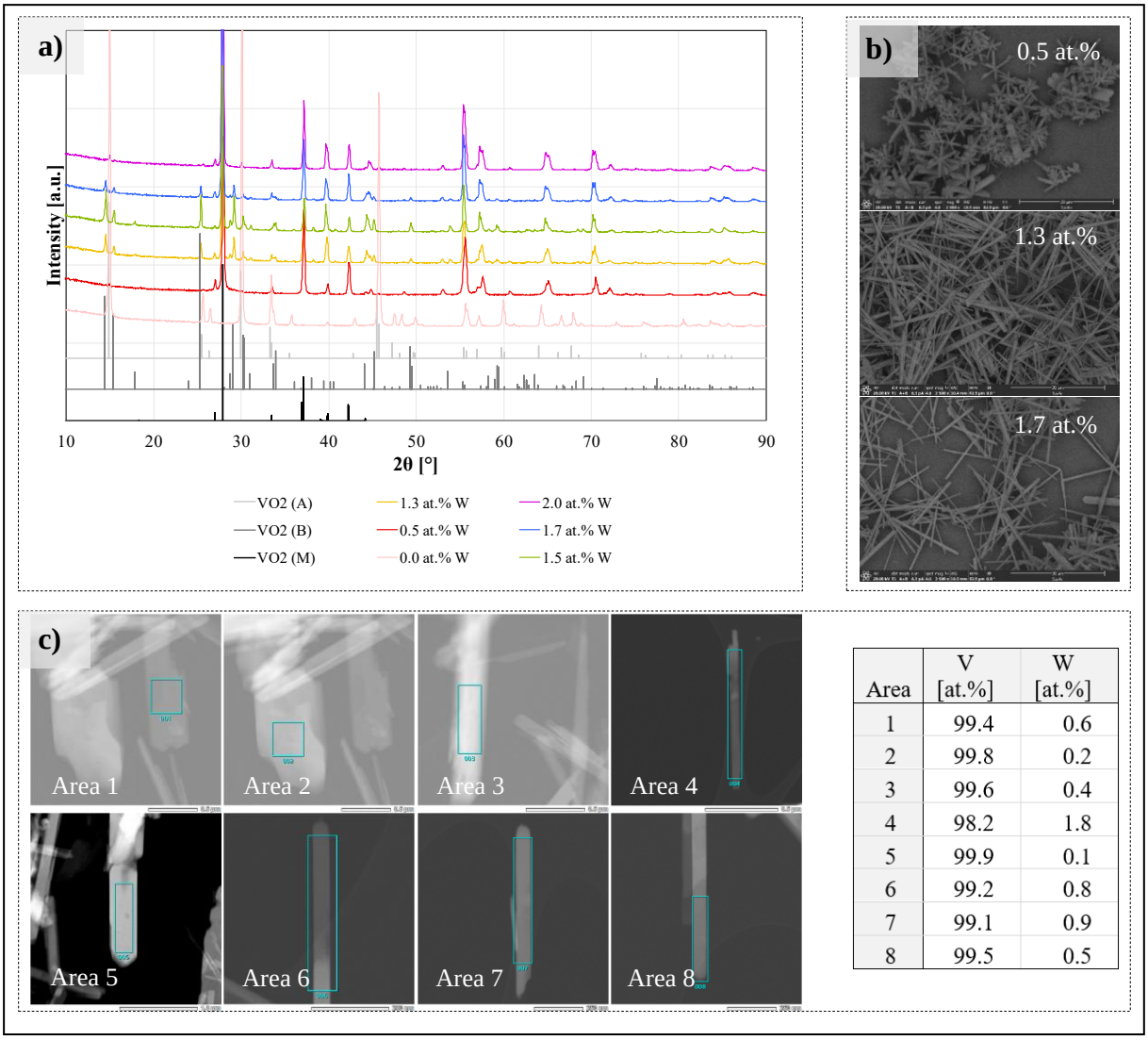

Area	V [at.%]	W [at.%]
1	99.4	0.6
2	99.8	0.2
3	99.6	0.4
4	98.2	1.8
5	99.9	0.1
6	99.2	0.8
7	99.1	0.9
8	99.5	0.5

Figure 4. a) XRD diffractogram of hydrothermally synthesized W/VO_2 particles obtained at a heating after 72h in a rotating autoclave at 230 °C, with the addition of different amount of W-dopant, with reference spectra for VO_2 (M) (PDF 72-0514), VO_2 (B) (PDF 31-1438), and VO_2 (A) (PDF 42-0876), b) SEM images obtained for the samples with 0.5 at.% W, 1.3 at.% W, and 1.7 at.% W added, c) HAADF-STEM images of VO2 particles synthesized with 1.5 at.% W, with regions analyzed by EDX marked in blue and a table revealing the compositions within each of these areas.

3.3 The thermokinetic analysis of hydrothermally synthesized W-doped VO_2 particles

Lastly, the kinetics of the thermochromic switch of vanadium dioxide (VO_2) from the monoclinic (M) to the tetragonal (R) structure, and *vice versa*, were investigated, as these are crucial for its application in smart windows. This transition is governed by the thermodynamic and kinetic parameters, including the switching enthalpy, switching temperature, and activation energy. The speed at which the transition occurs determines the efficiency of VO_2-based smart windows, particularly in regions with specific climatic conditions where rapid switching is necessary.[5,13]

The structural phase transition (SPT) of VO_2 is a complex, multi-step process that can be analyzed using isoconversional computational methods. Among these, the Friedman differential isoconversional method and the Ozawa-Flynn-Wall method are widely used to determine the activation energy as a function of conversion. Since the activation energy may vary with the extent of conversion, these methods provide a more detailed understanding of the kinetics involved. In the following analysis, the Friedman method will be applied to investigate the kinetic behavior of the SPT in VO_2.[5]

During the phase transition from VO_2 (M) to VO_2 (R), small nuclei of the tetragonal phase begin to form within the monoclinic structure in a process known as nucleation. As these nuclei grow and aggregate, the new phase expands until homogeneity is achieved. This transition only occurs when the material is heated above a critical temperature (T_0), as the nuclei of VO_2 (R) must overcome an energy barrier. Similarly, the reverse transition from VO_2 (R) to VO_2 (M) requires cooling below T_0 to overcome the energy barrier in the opposite direction.[5] Note that in the upcoming analysis, the focus is on the kinetics of nucleation, with the assumption that the rate-determining step is the nucleation process itself, rather than the subsequent growth of the nuclei.[19]

Nucleation in solids is influenced by impurities and defects, which facilitate diffusion and aggregation within the lattice. In the case of VO_2, vanadium ions diffuse along the V-V direction, playing a key role in the phase transition dynamics. The kinetics of this transition can be described by a single-step kinetic equation based on Arrhenius' Law, which is commonly used in thermal analysis to model reaction rates. This approach provides a quantitative framework to evaluate the rate at which VO_2 undergoes its thermochromic switching.[5]

$$\frac{d\alpha}{dt} = A\, exp\left(\frac{-E}{RT}\right) f(\alpha) \quad (1)$$

Here $d\alpha/dt$ is the rate of conversion, A is a temperature independent pre-exponential factor, E is the activation energy of the SPT, R is the gas constant, T is temperature, t is time, $f(\alpha)$ is the reaction model, and α is the degree of conversion with a value between zero and one. To obtain conversion rate data at the same extent of conversion, multiple heating rates (β) can be used:

$$\frac{d\alpha}{dt} = \beta \frac{d\alpha}{dt} \quad (2)$$

As the isoconversional principle states that the reaction rate solely depends on the temperature at a constant extent of conversion, the following expression for the activation energy E_a is obtained[5]:

$$E_a = -R\left(\frac{d\ln(d\alpha/dt)}{dT^{-1}}\right)_\alpha \quad (3)$$

Rearranging equation (1) by implementing this formulation of the activation energy results in the foundation of the Friedman differential isoconversional method[5]:

$$-R\ln\left(\frac{d\alpha}{dt}\right)_{\alpha,i} = -R\ln\left(A_\alpha f(\alpha)\right) + \frac{E_\alpha}{T_{\alpha,i}} \quad (4)$$

Where, i indicates the different heating and cooling rates applied, A_α is the pre-exponential factor at a specific extent of conversion (α), and $T_{\alpha,i}$ is the temperature at a specific extent of conversion (α) and at specific heating rate (i). Plotting $-R\ln(d\alpha/dt)$ as a function of T^{-1} results in the Friedman plot, where the activation energy corresponds to the gradient of the plot. In the context of nucleation, this activation energy represents the free energy barrier (ΔG^*) required for the formation of a new nucleus. As the nucleus reaches a critical radius, it surpasses this energy barrier and can subsequently grow spontaneously. Assuming homogeneous nucleation and a spherical nucleus, ΔG^* can be expressed mathematically in the following manner[5]:

$$\Delta G^* = \frac{16\pi\sigma^3 T_0^2}{3(\Delta H)^2(\Delta T)^2} = \frac{A}{(\Delta T)^2} \quad (5)$$

Where, T_0 is the critical switching temperature, ΔH is the phase transition enthalpy, and σ is the surface energy of the nucleus. These three parameters are combined into one integrated constant

A as these are material constants. ΔT represents the difference between the temperature of the material T and the critical temperature T_0, and is defined as $\Delta T = T - T_0$ for heating and $\Delta T = T_0 - T$ for cooling. For consistency reasons, the value of T_0 is taken at a conversion of 2% and is referred to as $T_{\alpha = 0.02}$. The nucleation rate has a complicated dependence on temperature, since ΔG^* depends on ΔT. As a result, the Friedman plot gives a non-linear relationship which is in contrast with Arrhenius plots for conventional chemical reactions. Derivation of equation (4) and substitution into equation (3) gives the following two equations for the activation energy, with E_h representing the activation energy for the transition of VO_2 (M) to VO_2 (R) and E_c representing the activation energy the transition from VO_2 (R) to VO_2 (M)[5]:

$$E_h = A\left(\frac{1}{(\Delta T)^2} + \frac{2T}{(\Delta T)^3}\right) \; or \; E_c = A\left(\frac{1}{(\Delta T)^2} - \frac{2T}{(\Delta T)^3}\right) \tag{6}$$

In this study, the extent of conversion is defined as the fractional enthalpy of the DSC peak, which results in the definition of the nucleation rate[5]:

$$\frac{d\alpha}{dt} = \frac{dH}{A_T dt} \tag{7}$$

Where, H is enthalpy of the phase transition, and A_T is the area under the entire thermogram, which corresponds to the enthalpy of the entire phase transition. The single-step equation is only applicable to the specific α which occurs in the temperature range of ΔT, therefore the kinetics of the entire process is a combination of many single-step kinetic equations. This also means that E_α depends on the conversion as it is not constant, and therefore, the constant value of $\alpha = 0.50$ is used in this study as the nucleation is considered homogeneous at this point.[5]

To investigate the kinetics of the solid-phase transformation (SPT) of VO_2 particles, DSC analyses were performed at various heating rates of 2.5, 5, 10, 15, and 20 °C·min^{-1}. By processing the obtained DSC profiles (**Figure S5, Table S5**), conversion-temperature (α-T) (**Figure S5**) and conversion-time (α-time) (**Figure S5**) profiles were generated. From the α-T profile, the temperature at which 50% conversion occurs ($T_{\alpha=0.50}$) was determined. The α-time profile enabled the calculation of the conversion rate at this 50% point by examining the first derivative of the conversion-time data between the 40% and 60% conversion marks.

These values, $T_{\alpha=0.50}$ and the conversion rate ($d\alpha/dt$) at $\alpha = 0.50$, were utilized to construct the Friedman plot (**Figure 5**), where the activation energy (E_a) (**Table 3**) was derived from the first

derivative of this plot. The results indicated that the activation energy for the phase transition between VO_2 (M) and VO_2 (R) is temperature-dependent, as revealed by the nonlinear relationship between $-R \ln(d\alpha/dt)$ and T^{-1}. Furthermore, the calculated activation energy represents an average value for multiple simultaneous phase transitions of species with varying W concentrations (see section 3.2). Notably, as the critical switching temperature approaches T_0, the activation barrier for the SPTs increases, whereas an increase in ΔT corresponds to a decrease in the activation energy.

It is important to note that during the calculations, the data point obtained at a heating rate of 5 °C/min in the Friedman plots was excluded, as this particular point was identified as an outlier in both the cooling and warming trends for each concentration. As a result, the activation energy was consistently calculated using data points corresponding to temperature rates of 2.5 to 10 °C/min, 10 to 15 °C/min, and 15 to 20 °C/min.

The Friedman plot of VO_2 particles with 0.5 at.% W doping (**Figure 5a***) reveals the highest absolute value of the activation energy $|E_a|$ for the SPT from VO_2 (M) to VO_2 (R), measuring 1,529.32 kJ·mol^{-1} at ΔT = 6.53 °C (**Table 3**). This plot exhibits asymmetric behavior, with a significant decrease in $|E_a|$ from 1,529.32 kJ·mol^{-1} to 702.03 kJ·mol^{-1}, as ΔT increases from 6.53 °C to 7.48 °C, during the transition from VO_2 (M) to VO_2 (R). In contrast, for the transition from VO_2 (R) to VO_2 (M), $|E_a|$ decreases more moderately from 291.49 kJ·mol^{-1} to 170.79 kJ·mol^{-1}, with an increase in ΔT from 17.30 °C to 20.08 °C.

For the 1.3 at.% W-doped VO_2 particles, the Friedman plot (**Figure 5b***) again indicates the highest $|E_a|$ for the SPT from VO_2 (M) to VO_2 (R), with a value of 1,568.48 kJ·mol^{-1} at ΔT = 18.68 °C (**Table 3**). Compared to the VO_2 particles with 0.5 at.% W doping, a much larger ΔT is required to reach a similar activation energy (18.68 °C vs. 6.53 °C). This plot also shows a kinetic asymmetry, with a sharp decrease in $|E_a|$ from 1,568.48 kJ·mol^{-1} to 392.04 kJ·mol^{-1} for the transition from VO_2 (M) to VO_2 (R) accompanied by an increase in ΔT of 0.75 °C (from 18.68 °C to 19.43 °C). Meanwhile, for the transition from VO_2 (R) to VO_2 (M), $|E_a|$ decreases from 721.21 kJ·mol^{-1} to 294.63 kJ·mol^{-1}, with an increase in ΔT of 0.97 °C (from 13.90 °C to 14.87 °C). In addition, the Friedman plot obtained for VO_2 particles with 1.7 at.% W (**Figure 5d***) doping reflects a pattern similar to that observed for the 1.3 at.% W doping, with the transition from VO_2 (M) to VO_2 (R) displaying the most significant decrease in $|E_a|$ from 3,258.48 kJ·mol^{-1} to 1,599.68 kJ·mol^{-1} with ΔT increasing from 35.12 to 35.81 °C (**Table 3**).

The reversed transition shows a decrease in $|E_a|$ from 1,029.38 kJ·mol^{-1} to 574.39 kJ·mol^{-1} with ΔT increasing from 15.41 to 16.25 °C.

In the case of VO_2 particles with 1.5 at.% W doping, the Friedman plot (**Figure 5c***) shows a more symmetrical relationship between the transitions from VO_2 (M) to VO_2 (R) and *vice versa*. Specifically, $|E_a|$ decreases by 2,298.21 kJ·mol^{-1} for the transition from monoclinic to rutile and by 2,663.33 kJ·mol^{-1} for the reverse transition (**Table 3**). However, for both transitions, ΔT experiences a slight decrease as $|E_a|$ decreases. This unforeseen trend requires additional examination. For VO_2 particles with a W concentration of 2.0 at.%, the highest activation energies are observed during the SPT from VO_2 (M) to VO_2 (R), with $|E_a|$ decreasing from 3,261.15 kJ·mol^{-1} to 588.70 kJ·mol^{-1} as ΔT increases (**Figure 5e***, **Table 3**). For the reverse transition from VO_2 (R) to VO_2 (M), $|E_a|$ decreases again with increasing ΔT.

Overall, the analysis of the kinetics of the thermochromic switch of VO_2 particles resulted in some notable observations. First, a distinct relationship between $|E_a|$ and ΔT is present, as $|E_a|$ decreases with increasing ΔT, along with a sharp increase in $|E_a|$ as ΔT approaches zero. This reflects the critical role of nucleation as the rate-determining step in the SPT, confirming the earlier assumption. Next, excluding the 1.5 at.% W-doped samples, the Friedman plots indicate a kinetic asymmetry, exhibiting a higher activation energy for the transition from VO_2 (M) to VO_2 (R) compared to the activation energy required for the transition from VO_2 (R) to VO_2 (M). Consequently, the transition from the monoclinic phase to the rutile phase is more challenging than the transition in the opposite direction. Lastly, across the entire dataset, $|E_a|$ tends to increase for both phase transitions with increasing concentration of W-dopant. These findings highlight important characteristics of the materials' switching behavior and the influence of doping levels on their kinetics.

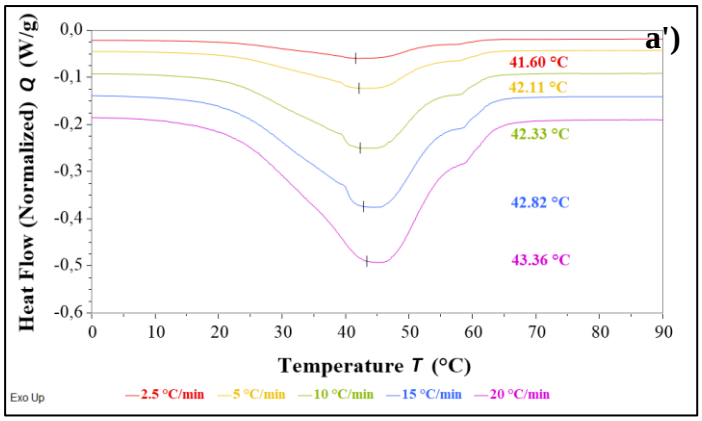
a')
41.60 °C
42.11 °C
42.33 °C
42.82 °C
43.36 °C
Heat Flow (Normalized) Q (W/g)
Temperature T (°C)
Exo Up
2.5 °C/min
5 °C/min
10 °C/min
15 °C/min
20 °C/min

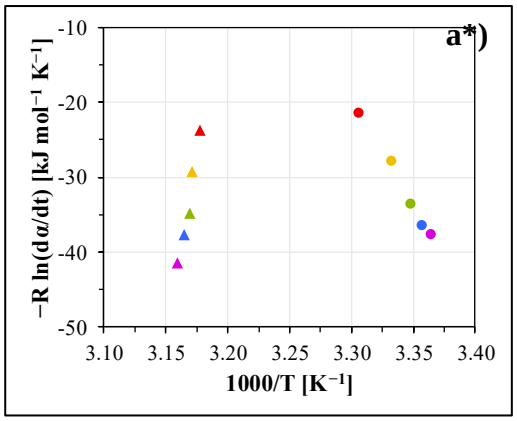
a*)
−R ln(dα/dt) [kJ mol⁻¹ K⁻¹]
1000/T [K⁻¹]

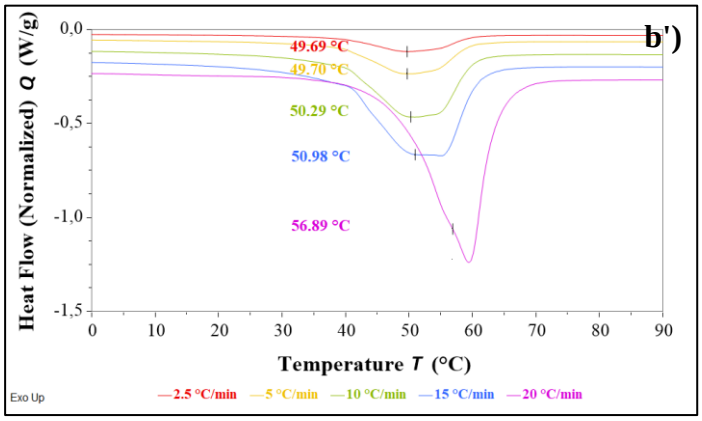
b')
49.69 °C
49.70 °C
50.29 °C
50.98 °C
56.89 °C
Heat Flow (Normalized) Q (W/g)
Temperature T (°C)
Exo Up
2.5 °C/min
5 °C/min
10 °C/min
15 °C/min
20 °C/min

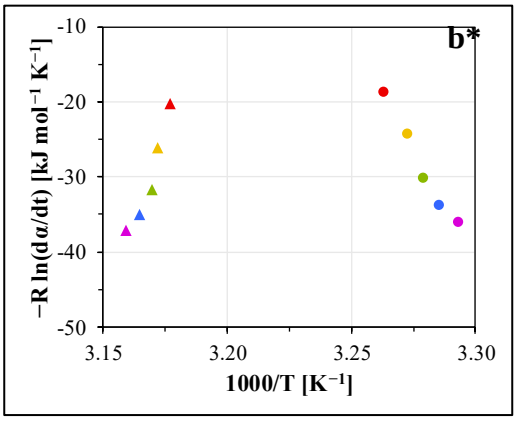
b*
−R ln(dα/dt) [kJ mol⁻¹ K⁻¹]
1000/T [K⁻¹]

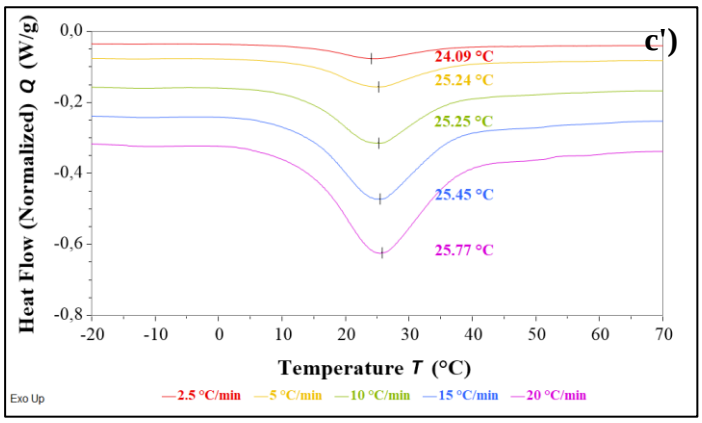
c')
24.09 °C
25.24 °C
25.25 °C
25.45 °C
25.77 °C
Heat Flow (Normalized) Q (W/g)
Temperature T (°C)
Exo Up
2.5 °C/min
5 °C/min
10 °C/min
15 °C/min
20 °C/min

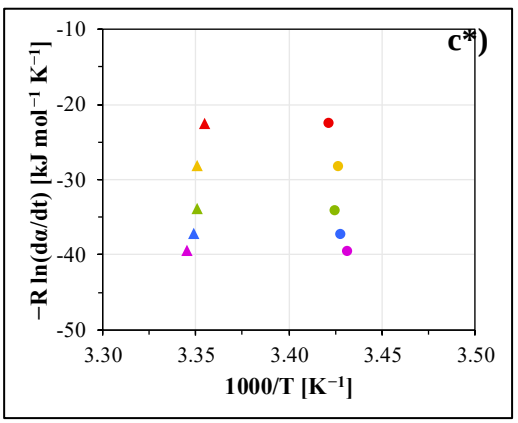
c*)
−R ln(dα/dt) [kJ mol⁻¹ K⁻¹]
1000/T [K⁻¹]

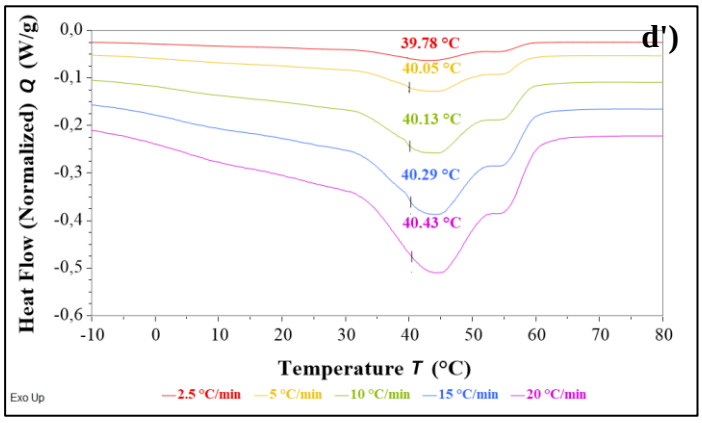
d')
39.78 °C
40.05 °C
40.13 °C
40.29 °C
40.43 °C
Heat Flow (Normalized) Q (W/g)
Temperature T (°C)
Exo Up
2.5 °C/min
5 °C/min
10 °C/min
15 °C/min
20 °C/min

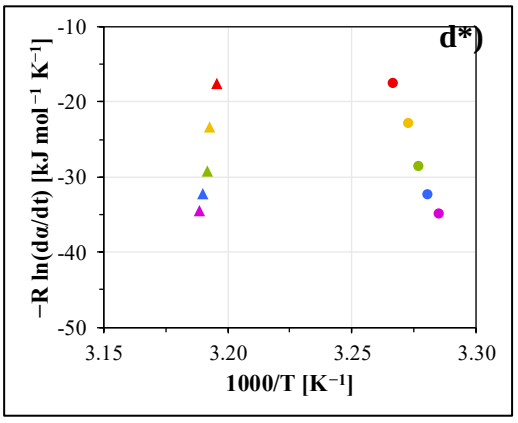
d*)
−R ln(dα/dt) [kJ mol⁻¹ K⁻¹]
1000/T [K⁻¹]

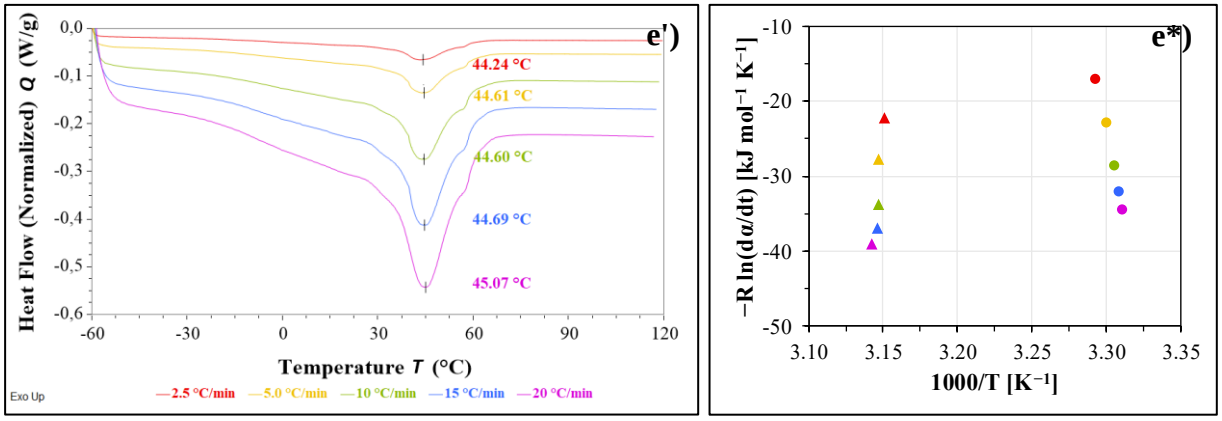

Figure 5. ') DSC heating curves obtained at different heating rates of hydrothermally synthesized W/VO_2 particles after 72h in a rotating autoclave at 230 °C, with the addition of a) 0.5 at.% W, b) 1.3 at.% W, c) 1.5 at.% W, d) 1.7 at.% W, and e) 2.0 at.% W, the indicated values corresponding to the temperature at 50% conversion ($T_{\alpha=0.50}$), *) the corresponding Friedman plots at 50% conversion for the VO_2 (M) to VO_2 (R) SPT (indicated by triangles) and the VO_2 (R) to VO_2 (M) SPT (indicated by dots).

Table 3. Activation energy (E_a), and ΔT for VO_2 particles with 0.5, 1.3, 1.5, 1.7, and 2.0 at.% W at heating and cooling rates of 2.5, 10, and 15 °C/min.

	0.5 at.% W (heating)		1.3 at.% W (heating)		1.5 at.% W (heating)		1.7 at.% W (heating)		2.0 at.% W (heating)	
T rate [°C/min]	*Ea* [kJ/mol]	ΔT	*Ea* [kJ/mol]	ΔT	*Ea* [kJ/mol]	ΔT	*Ea* [kJ/mol]	ΔT	*Ea* [kJ/mol]	ΔT
2.5	1529.32	6.53	1568.48	18.68	2901.71	16.00	3258.48	35.12	3261.15	17.14
10	591.28	7.10	658.67	18.83	1503.71	14.77	1878.84	35.42	3546.84	17.24
15	702.03	7.48	392.04	19.43	603.50	14.73	1599.68	35.81	588.70	18.39
	0.5 at.% W (cooling)		1.3 at.% W (cooling)		1.5 at.% W (cooling)		1.7 at.% W (cooling)		2.0 at.% W (cooling)	
T rate [°C/min]	*Ea* [kJ/mol]	ΔT	*Ea* [kJ/mol]	ΔT	*Ea* [kJ/mol]	ΔT	*Ea* [kJ/mol]	ΔT	*Ea* [kJ/mol]	ΔT
2.5	-291.49	17.30	-721.21	13.90	-3288.44	13.00	-1029.38	15.41	-863.89	20.19
10	-301.82	18.93	-558.21	14.45	-1319.70	12.31	-1014.67	15.82	-1051.51	19.12
15	-170.79	20.08	-294.63	14.87	-625.11	12.95	-574.39	16.25	-975.40	19.60

4 Conclusion and Outlook

In this manuscript, the incorporation of tungsten as dopant in VO_2 was investigated. W-doped VO_2 particles were prepared via hydrothermal synthesis, starting from vanadyl oxalate and ammonium metatungstate hydrate as metallo-organic precursors.

Initial findings focused on the effect of static and rotating reaction setups on the particle size and switching performance of the produced W/VO_2 particles. SEM analyses showed a smaller size distribution for the particles obtained by rotation than those obtained under static conditions. The DSC analysis showed for both conditions a rather broad transition peak, indicating the presence of multiple W-doped VO_2 species, each with a different tungsten concentration. In addition, the DSC results revealed sharper phase transition signals for the samples synthesized under rotating conditions in comparison to those synthesized under static conditions, suggesting a narrower particle size distribution of W-doped VO_2 species upon rotating. This finding was supported by the DSC results, showing that samples synthesized under rotational conditions exhibit narrower DSC peaks during the structural phase transition between VO_2 (M) and VO_2 (R) and *vice versa*. As these findings revealed that rotating conditions during the hydrothermal synthesis improves the particle size distribution and crystallinity, the subsequent experiments were performed using the rotation setup.

Hereafter, the study further examined the impact of different concentrations of tungsten dopant relative to the amount of vanadium, ranging from 0.0 at.% to 2.0 at.% W. Notably, not all experiments were replicable, which warrants caution in interpreting the results. DSC analyses indicated that undoped VO_2 transitioned at 170 °C, corresponding to VO_2 (A). The W-doped samples, particularly at concentrations between 0.5 and 1.5 at.%, exhibited a decrease in peak temperature, while those synthesized with 1.7 and 2.0 at.% W added, deviated from this trend, showing unexpectedly high peak temperature values. Anomalies in transition temperatures and broad DSC peaks pointed to non-uniform W distribution, highlighting the complexity of achieving uniform doping and the challenges posed by inhomogeneous distribution of the tungsten dopant. Furthermore, the study found no clear relationship between ΔH_{switch} and dopant concentration, with the highest enthalpy observed at 0.5 at.% W, while the 2.0 at.% W sample demonstrated a significant reduction in ΔH_{switch}, indicating lower crystal purity. TEM-EDX was performed to confirm the non-uniform incorporation of tungsten into the VO_2 particles.

Lastly, the manuscript delved into the thermokinetic analysis of the VO_2 phase transition of hydrothermally synthesized particles obtained under rotating conditions with varying amounts of W-dopant added to the samples. Employing the Friedman isoconversional method, the SPT and nucleation kinetics were analyzed, revealing three notable observations. The first finding confirmed that the nucleation behaves as the rate-determining step in the SPT by revealing a decrease in $|E_a|$ with an increase in ΔT and a sharp increase in $|E_a|$ as ΔT approached zero. Next, apart from the sample with 1.5 at.% W, the Friedman plots indicated a kinetic asymmetry, requiring a higher activation energy for the phase transition from VO_2 (M) to VO_2 (R) than for the opposite transition. Lastly, $|E_a|$ tended to increase with increasing concentration of W-dopant for both phase transitions.

Overall, this research emphasizes the nuanced challenges and potential of W-doped VO_2 particles, paving the way for future studies aimed at optimizing the synthesis process and reproducibility of the hydrothermal synthesis of W/VO_2 particles, as well as improving the incorporation of tungsten-dopant to obtain a homogeneous integration between the VO_2 (M) crystals. In addition, future research is required to reduce the particle size from the micrometer range to the nanometer range to allow the production of transparent coatings and film for thermochromic windows, essential to receive a great ΔT_{sol} in combination with a good value for T_{lum}.

5 Acknowledgements

I would like to express my sincere gratitude to several individuals and groups who contributed to the successful completion of this research.

First and foremost, I would like to thank Prof. Dr. Pascal Buskens and Prof. Dr. Marlies K. Van Bael for their invaluable conceptualization and supervision throughout this project. Their guidance in research and their ability to refine the course of this study were pivotal in navigating unforeseen challenges.

I would like to acknowledge Dr. Daniel Mann for his guidance, his insightful input that helped refine the define the focus of this research and his assistance with data interpretation, which greatly enriched the analysis presented in this work. My appreciation also goes to Dr. Ken Elen for his supervisory support, which facilitated a productive research environment.

A special thanks to Dr. Marcel A. Verheijen for his expertise in conducting the TEM and STEM-EDX analysis, which was critical to our findings. I also appreciate Mr. Luc Leufkens for his dedication in performing numerous DSC analyses, as well as SEM and XRD analyses, that contributed to the data quality. Additionally, I am grateful to Mr. Stijn Cosemans for providing additional samples that were essential for this research.

Lastly, I would like to thank the DESINe group for their guidance and support in the laboratory, which made this research possible.

This work would not have been possible without the collective effort and commitment of all mentioned, and I am sincerely appreciative of their contributions.

6 References

1. European Union. Energy efficient buildings. *Energy Performance of Buildings Directive* (2023).

2. IEA. *Net Zero by 2050*. (2021).

3. Li, M., Magdassi, S., Gao, Y. & Long, Y. Hydrothermal synthesis of VO2 polymorphs: advantages, challenges and prospects for the application of energy efficient smart windows. *SMALL* **13**, (2017).

4. TNO & Brightlands Chemelot Campus. Brightlands materials center. *Sustainable Buildings* (2024).

5. CALVI, L. VO2 nanoparticles and their application in thermochromic coatings and films for smart windows: An in-depth study of the thermodynamics and kinetics of the structural phase transition. (2024).

6. Timmers, K. *et al.* Hydrothermal synthesis of monoclinic VO2 microparticles without use of hazardous reagents: a key role for the W-dopant. *Inorg Chem* **63**, 5400–5413 (2024).

7. Liu, K., Lee, S., Yang, S., Delaire, O. & Wu, J. Recent progresses on physics and applications of vanadium dioxide. *Materials Today* **21**, 875–896 (2018).

8. Cui, Y. *et al.* Thermochromic VO2 for energy-efficient smart windows. *Joule* **2**, 1707–1746 (2018).

9. Morin, F. J. Oxides which show a metal-to-insulator transition at the Neel temperature. *Phys Rev Lett* **3**, 34–36 (1959).

10. Goodenough, J. B. The two components of the crystallographic transition in VO2. *J Solid State Chem* **3**, 490–500 (1971).

11. Jiang, C. *et al.* Phase-change VO2-based thermochromic smart windows. *Light: Science & Applications 2024 13:1* **13**, 1–22 (2024).

12. Wu, Y. *et al.* Depressed transition temperature of WxV1−xO2: mechanistic insights from the X-ray absorption fine structure (XAFS) spectroscopy. *Phys. Chem. Chem. Phys.* **16**, 17705–17714 (2014).

13. Zhang, H., Yu, H., Chen, Z., Luo, H. & Gao, Y. Thermal kinetic analysis of metal–insulator transition mechanism in W-doped VO2. *J Therm Anal Calorim* **126**, 949–957 (2016).

14. Zhang, Y., Xiong, W., Chen, W. & Zheng, Y. Recent progress on vanadium dioxide nanostructures and devices: fabrication, properties, applications and perspectives. *NANOMATERIALS* **11**, (2021).

15. Xu, F., Cao, X., Luo, H. & Jin, P. Recent advances in VO2-based thermochromic composites for smart windows. *J Mater Chem C Mater* **6**, 1903–1919 (2018).

16. Chang, T.-C. *et al.* Review on thermochromic vanadium dioxide based smart coatings: from lab to commercial application. *Adv Manuf* **6**, 1–19 (2018).

17. Calvi, L. *et al.* A comparative study on the switching kinetics of W/VO2 powders and VO2 coatings and their implications for thermochromic glazing. *SOLAR ENERGY MATERIALS AND SOLAR CELLS* **224**, (2021).

18. Calvi, L. *et al.* The impact of bead milling on the thermodynamics and kinetics of the structural phase transition of VO2 particulate materials and their potential for use in thermochromic glazing. *SOLAR ENERGY MATERIALS AND SOLAR CELLS* **242**, (2022).

19. Calvi, L. *et al.* Thermochromic glass laminates comprising W/VO2 nanoparticles obtained by wet bead milling: an in-depth study of the switching performance. *SOLAR ENERGY MATERIALS AND SOLAR CELLS* **257**, (2023).

7 Supporting information

SI 1 Experimental procedure

Table S1.1. The measured quantities of vanadium(V) oxide (V_2O_5), oxalic acid ($C_2H_2O_4$), and ammonium metatungstate hydrate ($(NH_4)_6H_2W_{12}O_{40}\cdot H_2O$) used across various experiments. It includes specific measurements in millimoles, the number of equivalents for each substance, and the atomic percentage of doping achieved in the process.

	V_2O_5			$C_2H_2O_4$			$(NH_4)_6H_2W_{12}O_{40}\cdot H_2O$		
	m [g]	#mmol	# equiv.	m [g]	#mmol	# equiv.	m [g]	#mmol	at.% W
Static vs. Rotating									
2.0 at.% W static cond.	0.2027	1.114	1.000	0.1996	2.217	1.989	0.0120	0.004059	2.14
2.0 at.% W rotating cond.	0.2050	1.127	1.000	0.2071	2.300	2.041	0.0118	0.003991	2.08
Different at.% W-dopant (under rotating conditions)									
0.0 at.% W	0.2019	1.110	1.000	0.1985	2.205	1.986	0.0000	0.000000	0.00
0.5 at.% W	0.2012	1.106	1.000	0.1989	2.209	1.997	0.0028	0.000947	0.51
1.3 at.% W	0.2016	1.108	1.000	0.1999	2.220	2.003	0.0072	0.002441	1.30
1.5 at.% W	0.2016	1.108	1.000	0.1999	2.220	2.003	0.0083	0.002816	1.50
1.7 at.% W	0.2016	1.108	1.000	0.1999	2.220	2.003	0.0094	0.003191	1.70
2.0 at.% W	0.1974	1.085	1.000	0.2040	2.266	2.088	0.0097	0.003281	1.78
Thermokinetic analysis (under rotating conditions)									
0.5 at.% W	0.2012	1.106	1.000	0.1989	2.209	1.997	0.0028	0.000947	0.51
1.3 at.% W	0.2016	1.108	1.000	0.1999	2.220	2.003	0.0072	0.002441	1.30
1.5 at.% W	0.2016	1.108	1.000	0.1999	2.220	2.003	0.0083	0.002816	1.50
1.7 at.% W	0.2016	1.108	1.000	0.1999	2.220	2.003	0.0094	0.003191	1.70
2.0 at.% W	0.2050	1.127	1.000	0.2071	2.300	2.041	0.0118	0.003991	2.08

Figure S1.1. The setup used during the hydrothermal synthesis of W/VO_2 particles. Left: a wide-angle view of the furnace, highlighting its design, including a rotating device. Right: a detailed photo showing the arrangement of autoclaves within the furnace, showcasing both vertical static and horizontal rotating configurations.

SI 2 Scanning Electron Microscopy (SEM) analyses of 2.0 at.% W-doped VO_2 particles synthesized under static or rotating conditions

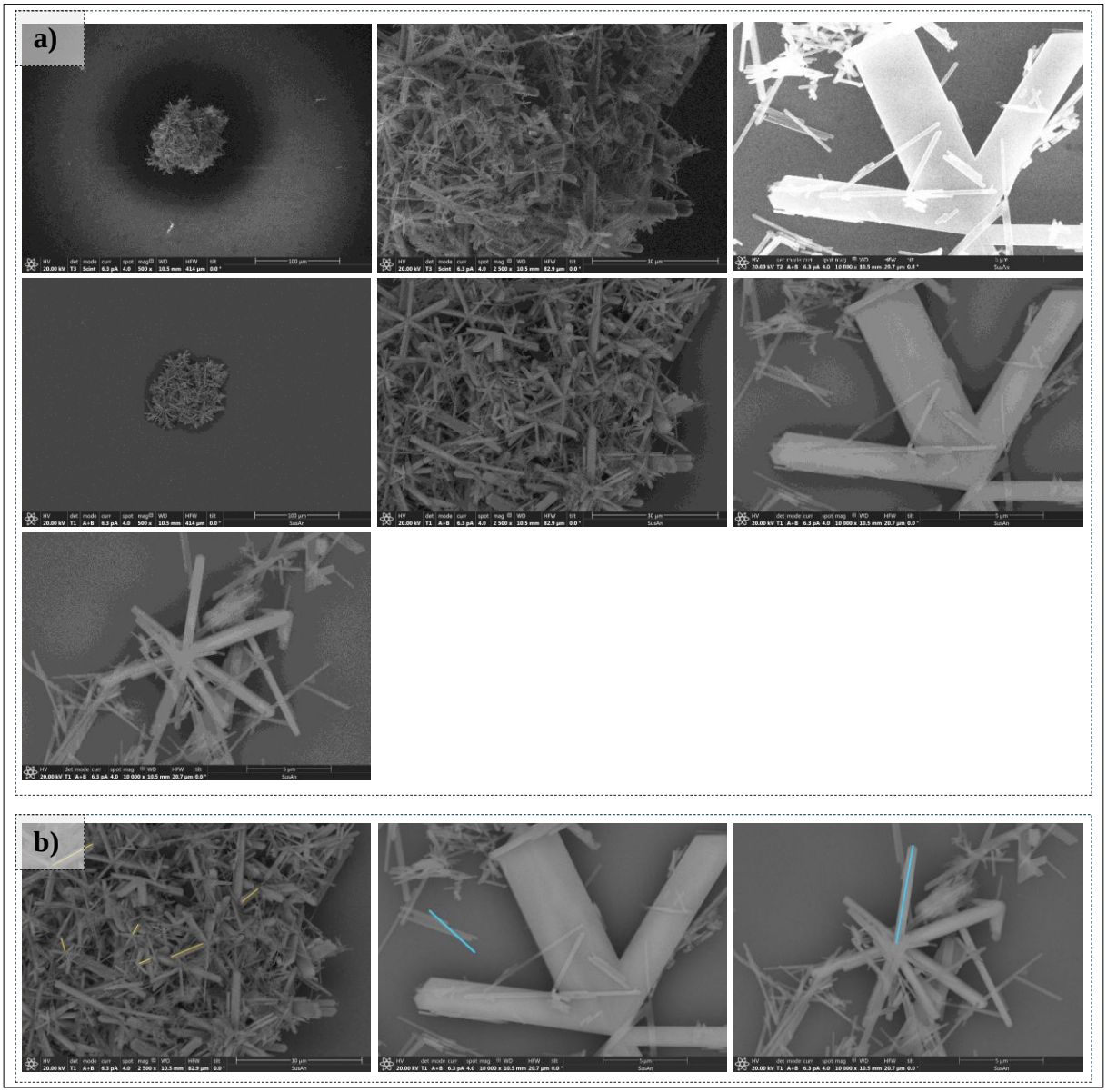

Figure S2.1. a) SEM images of 2.0 at.% W-doped VO_2 particles synthesized under rotating conditions b) SEM images with markings that were used to analyze the morphology of the obtained particles, yellow markings indicated fully formed VO_2 (M) asterisks, while blue markings represented either VO_2 (B) rods or partially formed VO_2 (M) asterisks.

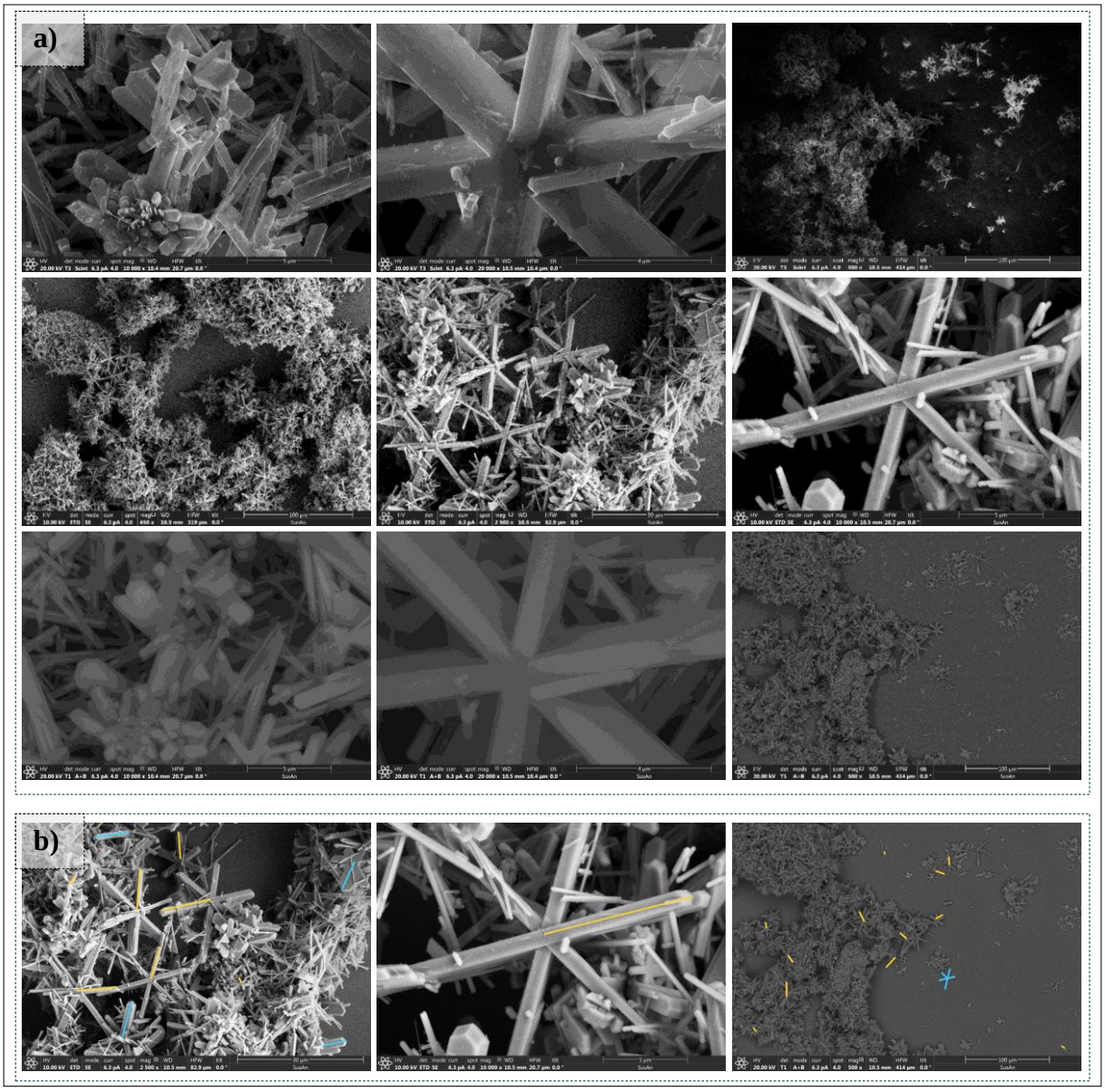

Figure S2.2. a) SEM images of 2.0 at.% W-doped VO_2 particles synthesized under static conditions b) SEM images with markings that were used to analyze the morphology of the obtained particles, yellow markings indicated fully formed VO_2 (M) asterisks, while blue markings represented either VO_2 (B) rods or partially formed VO_2 (M) asterisks.

SI 3 Differential scanning calorimetry (DSC) analyses of VO_2 particles with different concentrations of W-dopant synthesized under rotating conditions

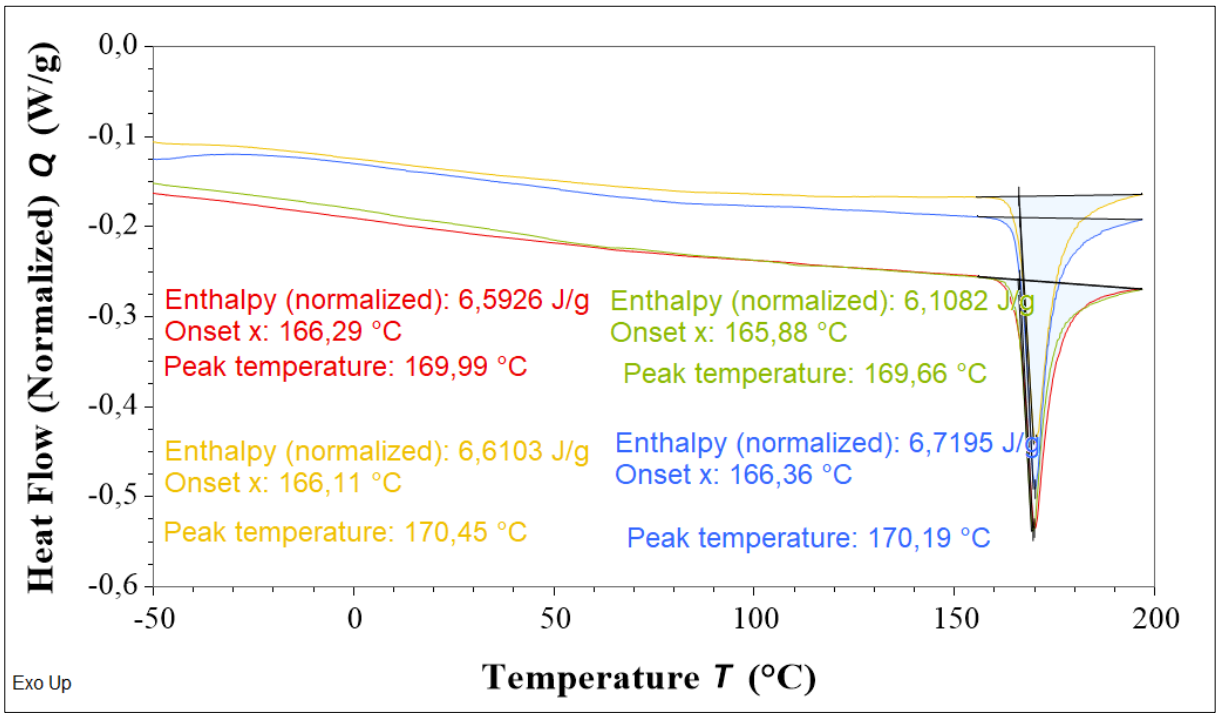

Figure S3.1. DSC results of four different undoped VO_2 samples hydrothermally synthesized for 72h at 230 °C under rotating conditions, showing the enthalpy, onset x, and peak temperature for their respective phase transitions

SI 4 Scanning Electron Microscopy (SEM) analyses of VO_2 particles with different concentrations of W-dopant synthesized under rotating conditions

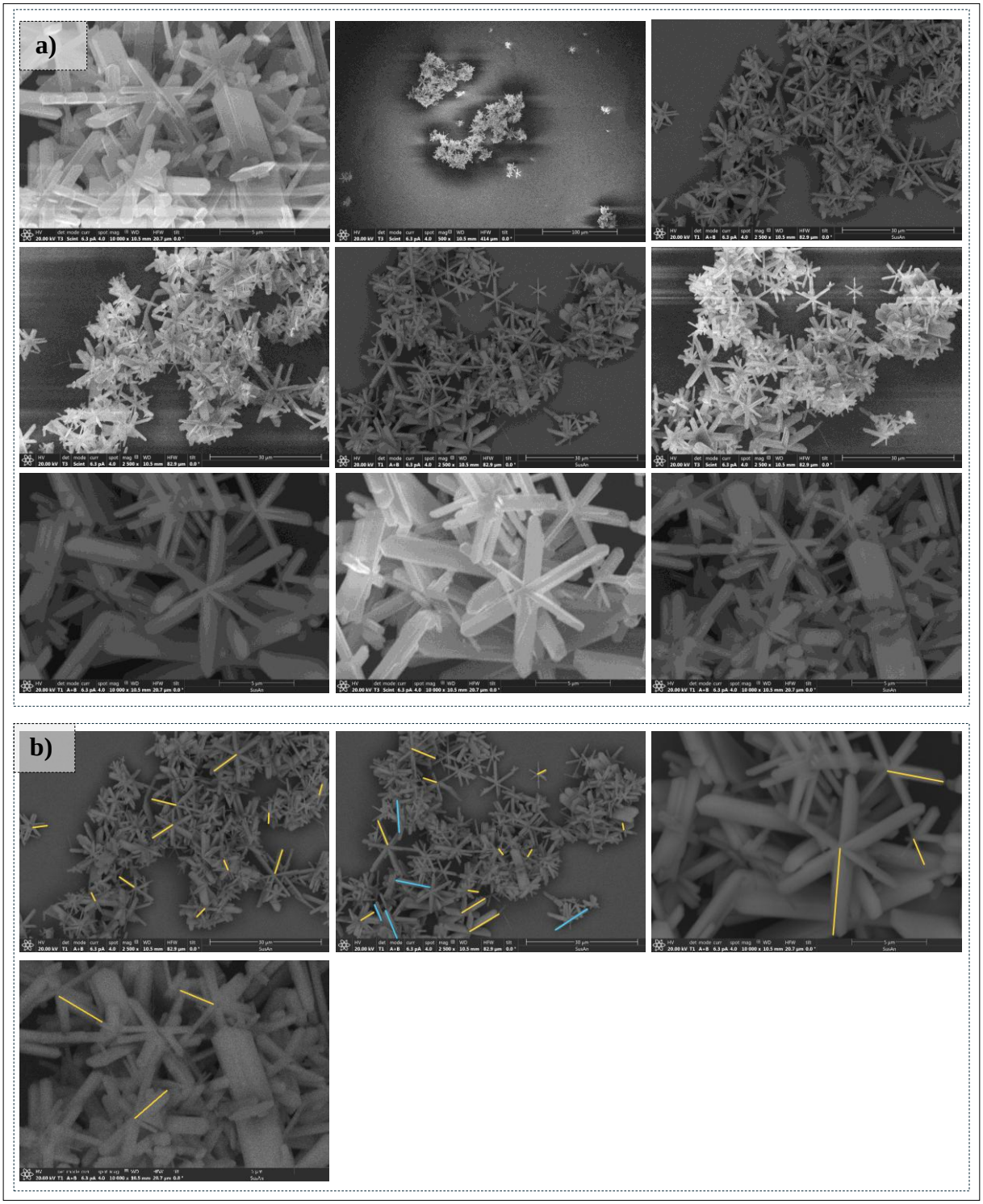

Figure S4.1. a) SEM images of 0.5 at.% W-doped VO_2 particles synthesized under rotating conditions b) SEM images with markings that were used to analyze the morphology of the obtained particles, yellow markings indicated fully formed VO_2 (M) asterisks, while blue markings represented either VO_2 (B) rods or partially formed VO_2 (M) asterisks.

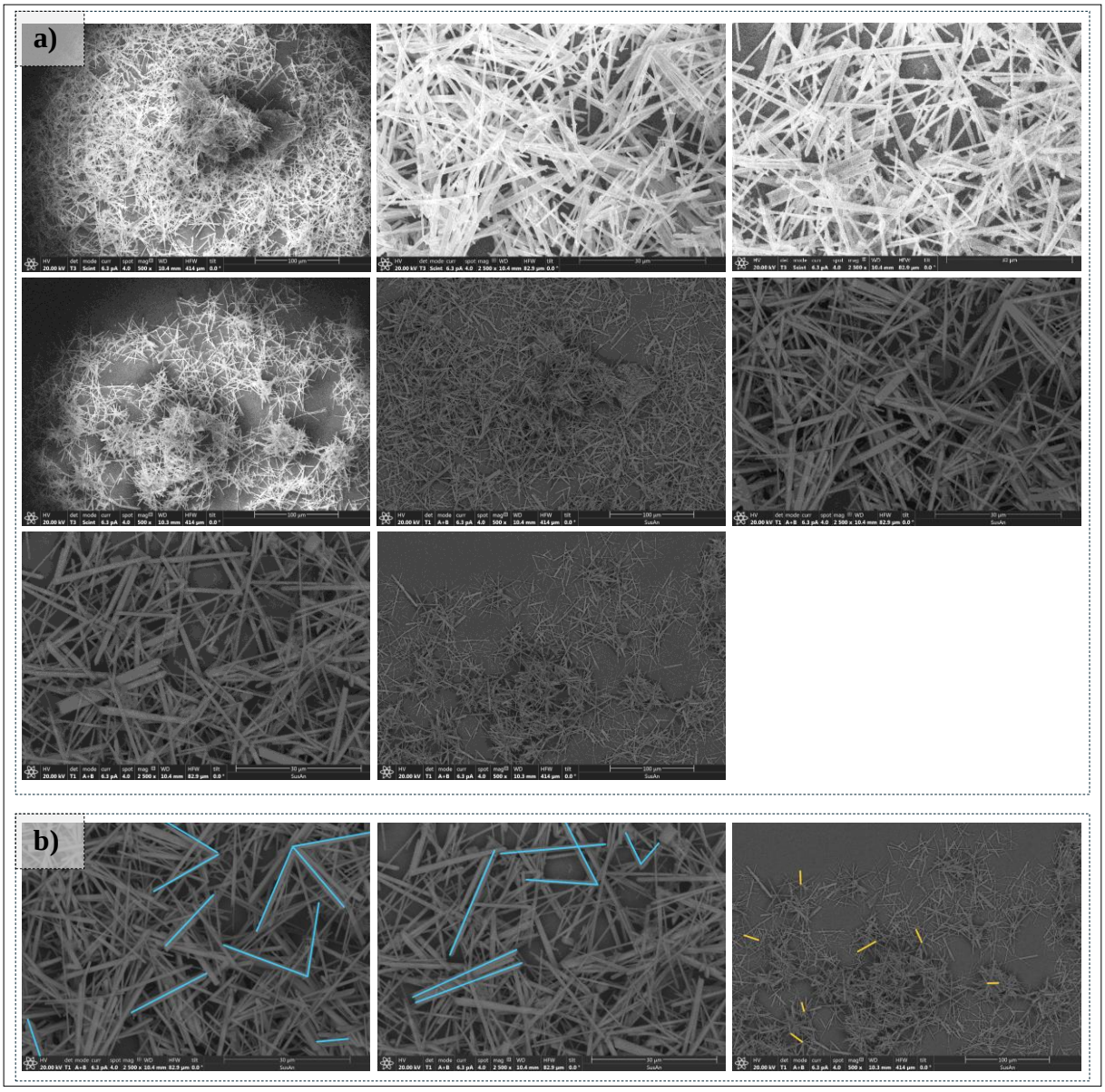

Figure S4.2. a) SEM images of 1.3 at.% W-doped VO_2 particles synthesized under rotating conditions b) SEM images with markings that were used to analyze the morphology of the obtained particles, yellow markings indicated fully formed VO_2 (M) asterisks, while blue markings represented either VO_2 (B) rods or partially formed VO_2 (M) asterisks.

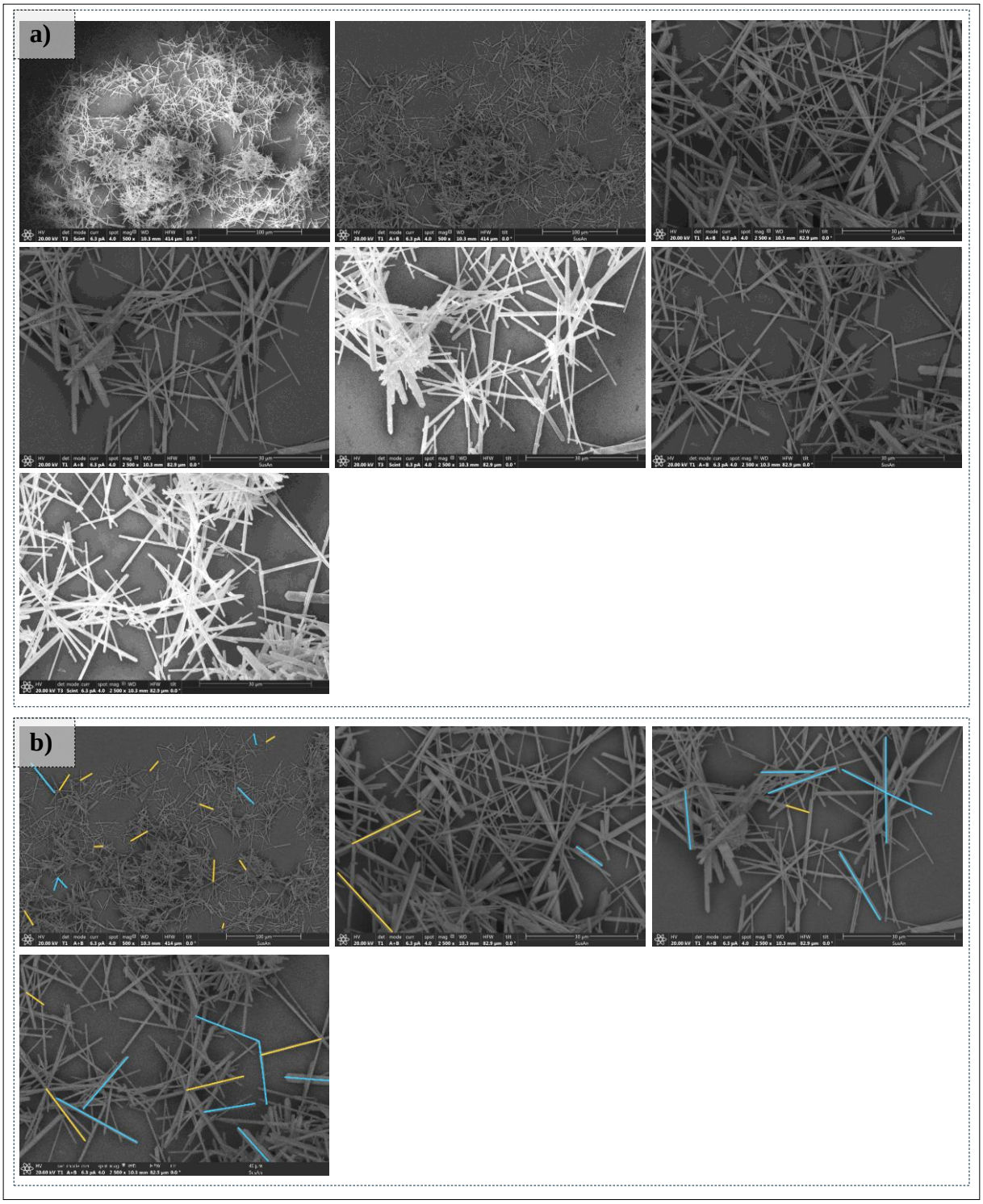

Figure S4.3. a) SEM images of 1.7 at.% W-doped VO_2 particles synthesized under rotating conditions b) SEM images with markings that were used to analyze the morphology of the obtained particles, yellow markings indicated fully formed VO_2 (M) asterisks, while blue markings represented either VO_2 (B) rods or partially formed VO_2 (M) asterisks.

SI 5 Differential Scanning Calorimetry (DSC) results of the thermokinetic analysis of VO_2 particles with different concentrations of W-dopant synthesized under rotating conditions

Table S5.1. The rate of conversion ($d\alpha/dt$), the temperature at 50% ($T_{0.50}$) and 2% ($T_{0.02}$) conversion, and ΔT of 0.5 at.% W-doped VO_2 particles obtained by DSC analysis using different heating rates, along with $-R\ \ln(d\alpha/dt)$ and $1000/T$ used to create Friedman plots, and the activation energy (E_a) derived from these graphs.

0.5 at.% W (heating)									
temp rate	dα/dt	−Rln(dα/dt) [J·mol^{-1}K^{-1}]	$T_{0.50}$ [°C]	$T_{0.50}$ [K]	1000/$T_{0.50}$ [K^{-1}]	$T_{0.02}$ [°C]	$T_{0.02}$ [K]	E_a [kJ/mol]	ΔT
2.5 °C/min	17.1465	-23.628	41.60	314.75	3.1771	35.07	308.22	1529.32	6.53
5 °C/min	34.1413	-29.354	42.11	315.26	3.1720	35.35	308.50		6.76
10 °C/min	66.2884	-34.871	42.33	315.48	3.1698	35.23	308.38	591.28	7.10
15 °C/min	94.0276	-37.778	42.82	315.97	3.1649	35.34	308.49	702.03	7.48
20 °C/min	148.339	-41.568	43.36	316.51	3.1595	41.20	314.35		
0.5 at.% W (cooling)									
temp rate	dα/dt	−Rln(dα/dt) [J·mol^{-1}K^{-1}]	$T_{0.50}$ [°C]	$T_{0.50}$ [K]	1000/$T_{0.50}$ [K^{-1}]	$T_{0.02}$ [°C]	$T_{0.02}$ [K]	E_a [kJ/mol]	ΔT
2.5 °C/min	13.1301	-21.409	29.31	302.46	3.3062	46.61	319.76	-291.49	17.30
5 °C/min	28.7451	-27.924	26.89	300.04	3.3329	44.98	318.13		18.09
10 °C/min	57.8319	-33.736	25.49	298.64	3.3485	44.42	317.57	-301.82	18.93
15 °C/min	81.4833	-36.587	24.65	297.80	3.3580	44.73	317.88	-170.79	20.08
20 °C/min	93.2236	-37.706	24.07	297.22	3.3645	45.63	318.78		

Table S5.2. The rate of conversion ($d\alpha/dt$), the temperature at 50% ($T_{0.50}$) and 2% ($T_{0.02}$) conversion, and ΔT of 1.3 at.% W-doped VO_2 particles obtained by DSC analysis using different heating rates, along with $-R\ \ln(d\alpha/dt)$ and $1000/T$ used to create Friedman plots, and the activation energy (E_a) derived from these graphs.

1.3 at.% W (heating)									
temp rate	dα/dt	−Rln(dα/dt) [J·mol^{-1}K^{-1}]	$T_{0.50}$ [°C]	$T_{0.50}$ [K]	1000/$T_{0.50}$ [K^{-1}]	$T_{0.02}$ [°C]	$T_{0.02}$ [K]	E_a [kJ/mol]	ΔT
2.5 °C/min	11.4773	-20.290	41.60	314.75	3.1771	22.92	296.07	1568.48	18.68
5 °C/min	23.2233	-26.150	42.11	315.26	3.1720	23.17	296.32		18.94
10 °C/min	45.9345	-31.821	42.33	315.48	3.1698	23.5	296.65	658.67	18.83
15 °C/min	67.8046	-35.059	42.82	315.97	3.1649	23.39	296.54	392.04	19.43
20 °C/min	87.4641	-37.176	43.36	316.51	3.1595	23.63	296.78		
1.3 at.% W (cooling)									
temp rate	dα/dt	−Rln(dα/dt) [J·mol^{-1}K^{-1}]	$T_{0.50}$ [°C]	$T_{0.50}$ [K]	1000/$T_{0.50}$ [K^{-1}]	$T_{0.02}$ [°C]	$T_{0.02}$ [K]	E_a [kJ/mol]	ΔT
2.5 °C/min	9.53916	-18.753	33.31	306.46	3.2631	47.21	320.36	-721.21	13.90
5 °C/min	18.8576	-24.419	32.4	305.55	3.2728	46.58	319.73		14.18
10 °C/min	38.3823	-30.328	31.81	304.96	3.2791	46.26	319.41	-558.21	14.45
15 °C/min	58.8118	-33.876	31.22	304.37	3.2855	46.09	319.24	-294.63	14.87
20 °C/min	77.8077	-36.203	30.49	303.64	3.2934	45.97	319.12		

Table S5.3. The rate of conversion ($d\alpha/dt$), the temperature at 50% ($T_{0.50}$) and 2% ($T_{0.02}$) conversion, and ΔT of 1.5 at.% W-doped VO_2 particles obtained by DSC analysis using different heating rates, along with $-R\ \ln(d\alpha/dt)$ and $1000/T$ used to create Friedman plots, and the activation energy (E_a) derived from these graphs.

1.5 at.% W (heating)									
temp rate	dα/dt	−Rln(dα/dt) [J·mol^{-1}K^{-1}]	$T_{0.50}$ [°C]	$T_{0.50}$ [K]	1000/$T_{0.50}$ [K^{-1}]	$T_{0.02}$ [°C]	$T_{0.02}$ [K]	E_a [kJ/mol]	ΔT
2.5 °C/min	14.9334	-22.479	24.90	298.05	3.3551	8.90	282.05	2901.71	16.00
5 °C/min	29.4541	-28.127	25.24	298.39	3.3513	9.29	282.44		15.95
10 °C/min	58.9685	-33.898	25.25	298.40	3.3512	10.48	283.63	1503.71	14.77
15 °C/min	88.4953	-37.273	25.45	298.60	3.3490	10.72	283.87	603.50	14.73
20 °C/min	114.798	-39.437	25.77	298.92	3.3454	10.43	283.58		
1.5 at.% W (cooling)									
temp rate	dα/dt	−Rln(dα/dt) [J·mol^{-1}K^{-1}]	$T_{0.50}$ [°C]	$T_{0.50}$ [K]	1000/$T_{0.50}$ [K^{-1}]	$T_{0.02}$ [°C]	$T_{0.02}$ [K]	E_a [kJ/mol]	ΔT
2.5 °C/min	15.1352	-22.591	19.08	292.23	3.4220	32.08	305.23	-3288.44	13.00
5 °C/min	30.3064	-28.364	18.66	291.81	3.4269	31.28	304.43		12.62
10 °C/min	60.8156	-34.155	18.78	291.93	3.4255	31.09	304.24	-1319.70	12.31
15 °C/min	89.9486	-37.409	18.57	291.72	3.4279	31.52	304.67	-625.11	12.95
20 °C/min	118.321	-39.688	18.26	291.41	3.4316	31.50	304.65		

Table S5.4. The rate of conversion ($d\alpha/dt$), the temperature at 50% ($T_{0.50}$) and 2% ($T_{0.02}$) conversion, and ΔT of 1.7 at.% W-doped VO_2 particles obtained by DSC analysis using different heating rates, along with $-R\ \ln(d\alpha/dt)$ and $1000/T$ used to create Friedman plots, and the activation energy (E_a) derived from these graphs.

1.7 at.% W (heating)									
temp rate	dα/dt	−Rln(dα/dt) [J·mol^{-1}K^{-1}]	$T_{0.50}$ [°C]	$T_{0.50}$ [K]	1000/$T_{0.50}$ [K^{-1}]	$T_{0.02}$ [°C]	$T_{0.02}$ [K]	E_a [kJ/mol]	ΔT
2.5 °C/min	8.32342	-17.619	39.78	312.93	3.1956	4.66	277.81	3258.48	35.12
5 °C/min	16.5901	-23.354	40.05	313.20	3.1928	4.55	277.70		35.50
10 °C/min	33.7248	-29.252	40.13	313.28	3.1920	4.71	277.86	1878.84	35.42
15 °C/min	48.7369	-32.314	40.29	313.44	3.1904	4.48	277.63	1599.68	35.81
20 °C/min	64.1024	-34.592	40.43	313.58	3.1890	4.45	277.60		
1.7 at.% W (cooling)									
temp rate	dα/dt	−Rln(dα/dt) [J·mol^{-1}K^{-1}]	$T_{0.50}$ [°C]	$T_{0.50}$ [K]	1000/$T_{0.50}$ [K^{-1}]	$T_{0.02}$ [°C]	$T_{0.02}$ [K]	E_a [kJ/mol]	ΔT
2.5 °C/min	8.3056	-17.601	33.00	306.15	3.2664	48.41	321.56	-1029.38	15.41
5 °C/min	15.8456	-22.972	32.37	305.52	3.2731	47.86	321.01		15.49
10 °C/min	31.6726	-28.730	31.99	305.14	3.2772	47.81	320.96	-1014.67	15.82
15 °C/min	49.4802	-32.440	31.65	304.80	3.2808	47.90	321.05	-574.39	16.25
20 °C/min	67.1454	-34.978	31.24	304.39	3.2853	47.91	321.06		

Table S5.5. The rate of conversion ($d\alpha/dt$), the temperature at 50% ($T_{0.50}$) and 2% ($T_{0.02}$) conversion, and ΔT of 2.0 at.% W-doped VO_2 particles obtained by DSC analysis using different heating rates, along with $-R\ \ln(d\alpha/dt)$ and $1000/T$ used to create Friedman plots, and the activation energy (E_a) derived from these graphs.

2.0 at.% W (heating)									
temp rate	dα/dt	−Rln(dα/dt) [J·mol^{-1}K^{-1}]	$T_{0.50}$ [°C]	$T_{0.50}$ [K]	1000/$T_{0.50}$ [K^{-1}]	$T_{0.02}$ [°C]	$T_{0.02}$ [K]	E_a [kJ/mol]	ΔT
2.5 °C/min	14.2961	-22.116	44.24	317.39	3.1507	27.10	300.25	3261.15	17.14
5 °C/min	28.5179	-27.858	44.61	317.76	3.1470	27.13	300.28		17.48
10 °C/min	57.9791	-33.758	44.60	317.75	3.1471	27.36	300.51	3546.84	17.24
15 °C/min	84.7946	-36.918	44.69	317.84	3.1462	26.30	299.45	588.70	18.39
20 °C/min	110.636	-39.130	45.07	318.22	3.1425	27.45	300.60		
2.0 at.% W (cooling)									
temp rate	dα/dt	−Rln(dα/dt) [J·mol^{-1}K^{-1}]	$T_{0.50}$ [°C]	$T_{0.50}$ [K]	1000/$T_{0.50}$ [K^{-1}]	$T_{0.02}$ [°C]	$T_{0.02}$ [K]	E_a [kJ/mol]	ΔT
2.5 °C/min	7.73519	-17.010	30.57	303.72	3.2925	50.76	323.91	-863.89	20.19
5 °C/min	15.9333	-23.018	29.83	302.98	3.3005	49.60	322.75		19.77
10 °C/min	31.8025	-28.764	29.32	302.47	3.3061	48.44	321.59	-1051.51	19.12
15 °C/min	47.5036	-32.101	29.03	302.18	3.3093	48.63	321.78	-975.40	19.60
20 °C/min	63.8489	-34.559	28.80	301.95	3.3118	48.75	321.90		

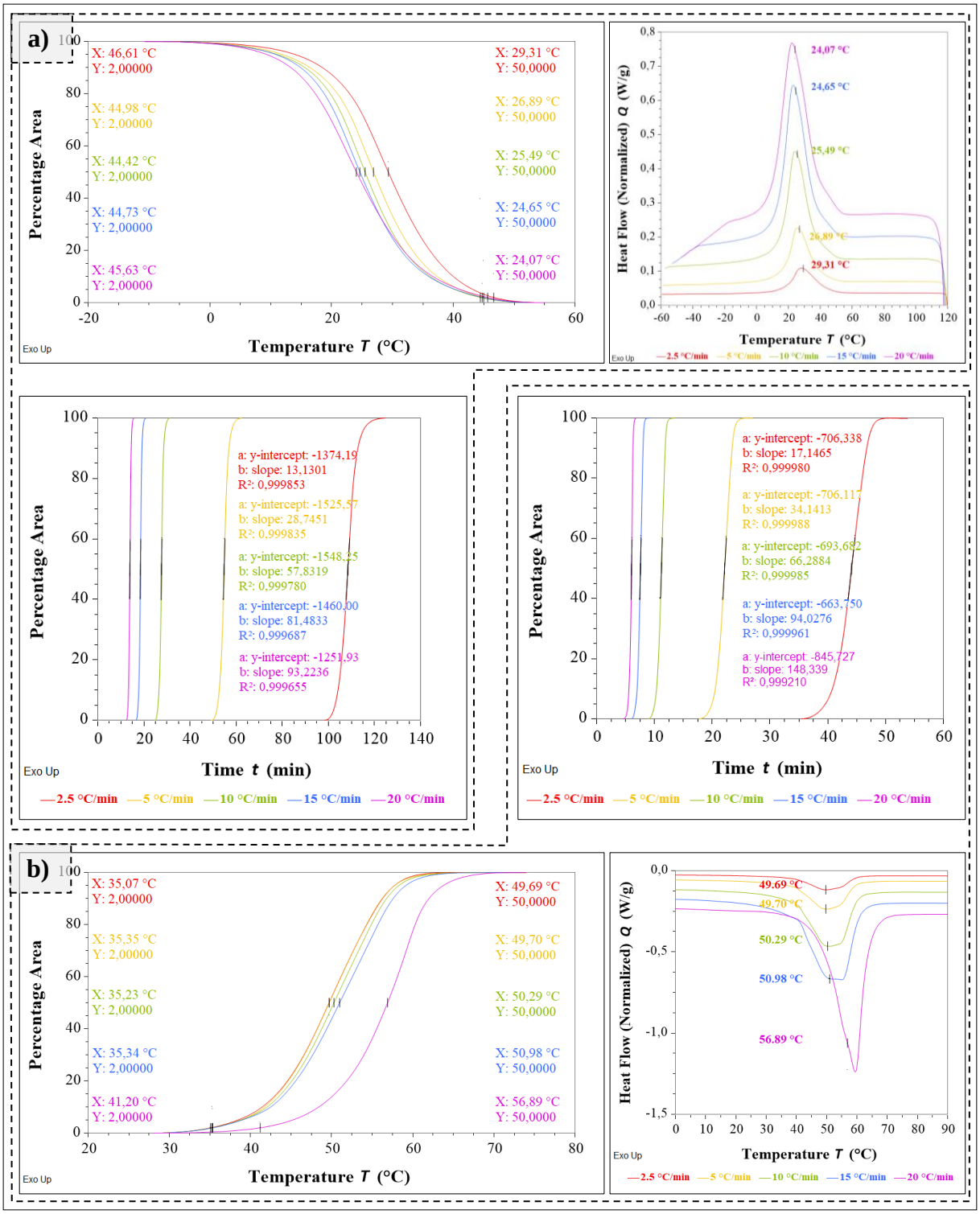

Figure S5.1. Conversion vs. temperature plot, heat flow vs. temperature plot, and conversion vs. time plot for the transition a) from VO_2 (R) to VO_2 (M) and b) from VO_2 (M) to VO_2 (R) for the particles with 0.5 at.% W-doping.

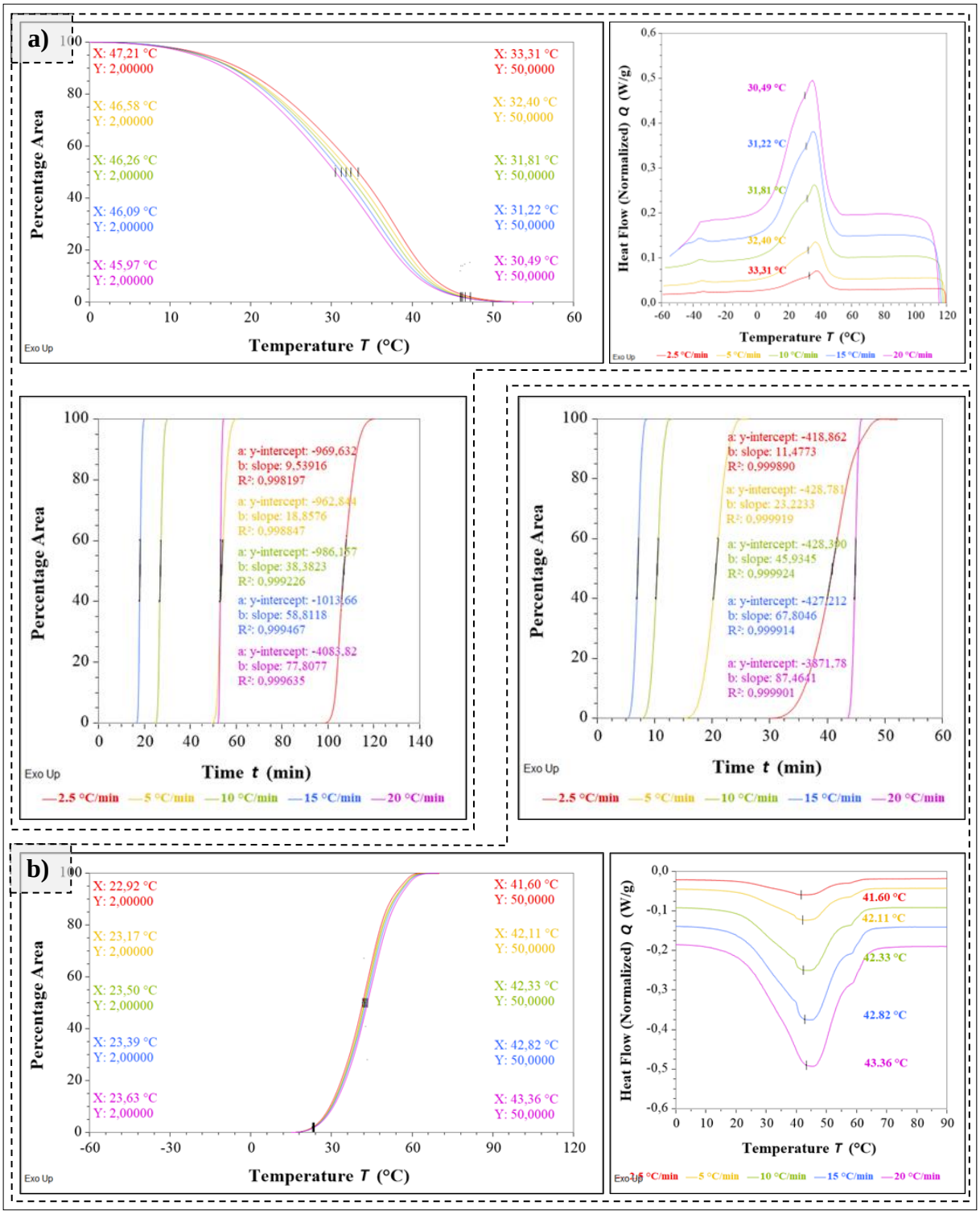

Figure S5.2. Conversion vs. temperature plot, heat flow vs. temperature plot, and conversion vs. time plot for the transition a) from VO_2 (R) to VO_2 (M) and b) from VO_2 (M) to VO_2 (R) for the particles with 1.3 at.% W-doping.

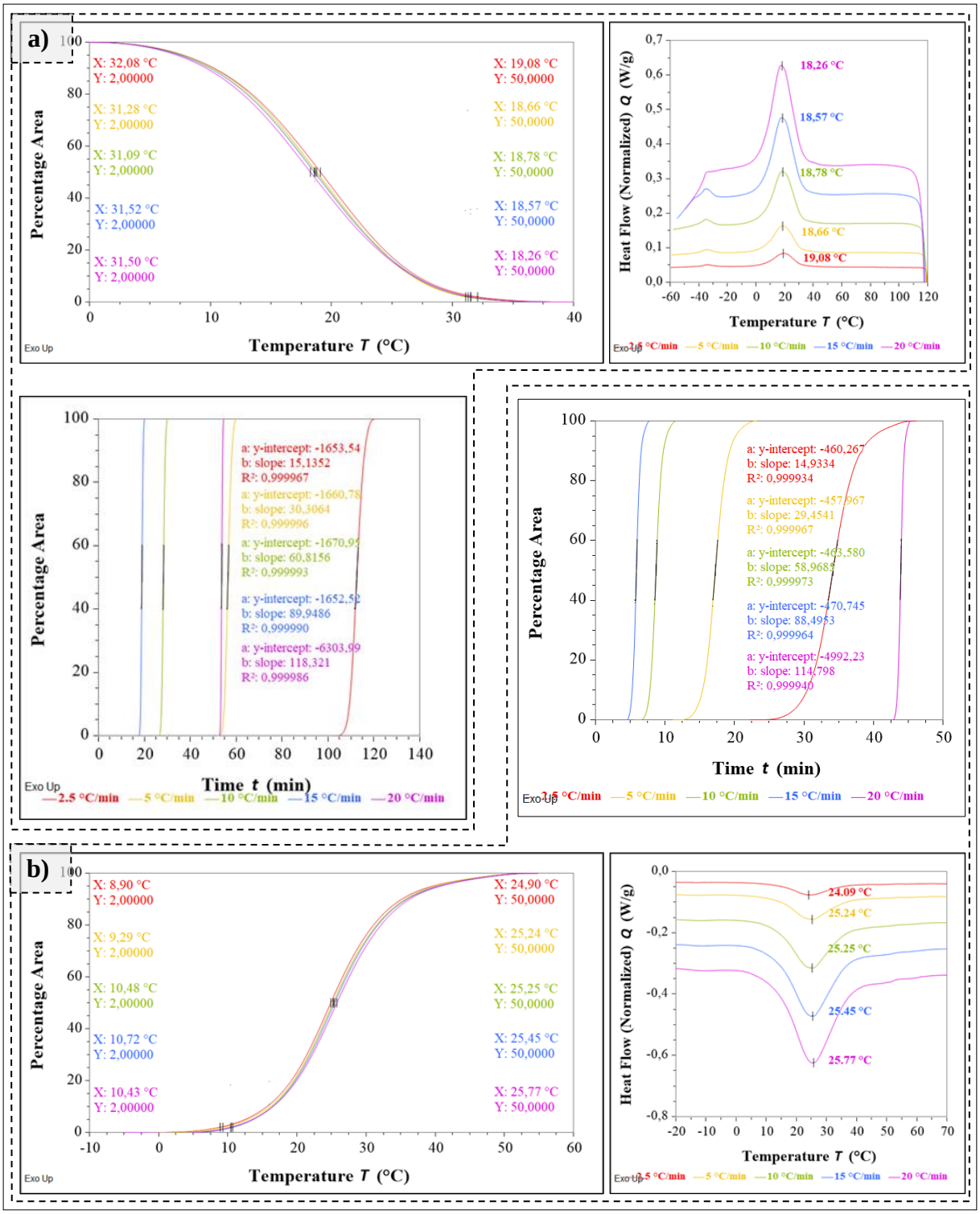

Figure S5.3. Conversion vs. temperature plot, heat flow vs. temperature plot, and conversion vs. time plot for the transition a) from VO_2 (R) to VO_2 (M) and b) from VO_2 (M) to VO_2 (R) for the particles with 1.5 at.% W-doping.

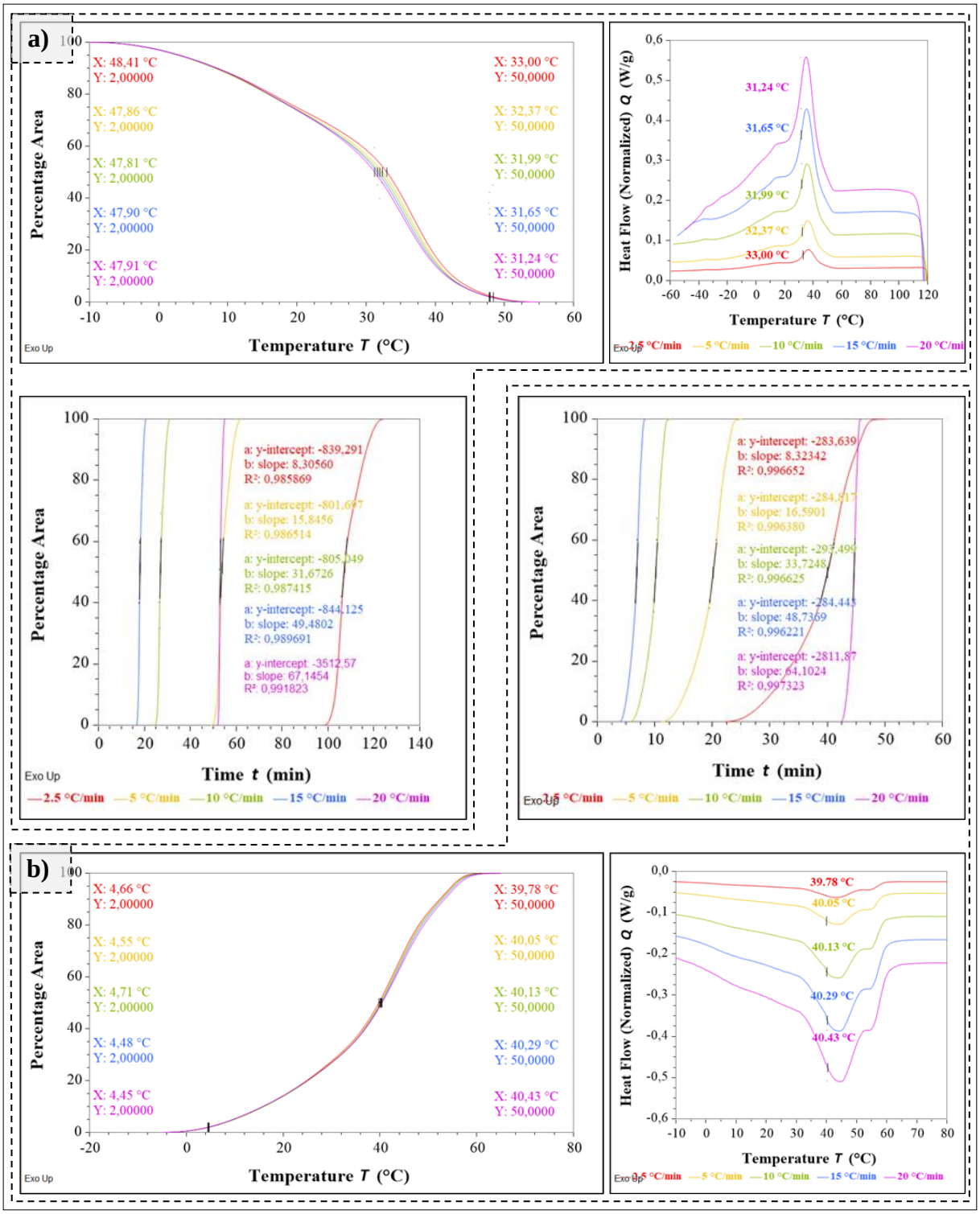

Figure S5.4. Conversion vs. temperature plot, heat flow vs. temperature plot, and conversion vs. time plot for the transition a) from VO_2 (R) to VO_2 (M) and b) from VO_2 (M) to VO_2 (R) for the particles with 1.7 at.% W-doping.

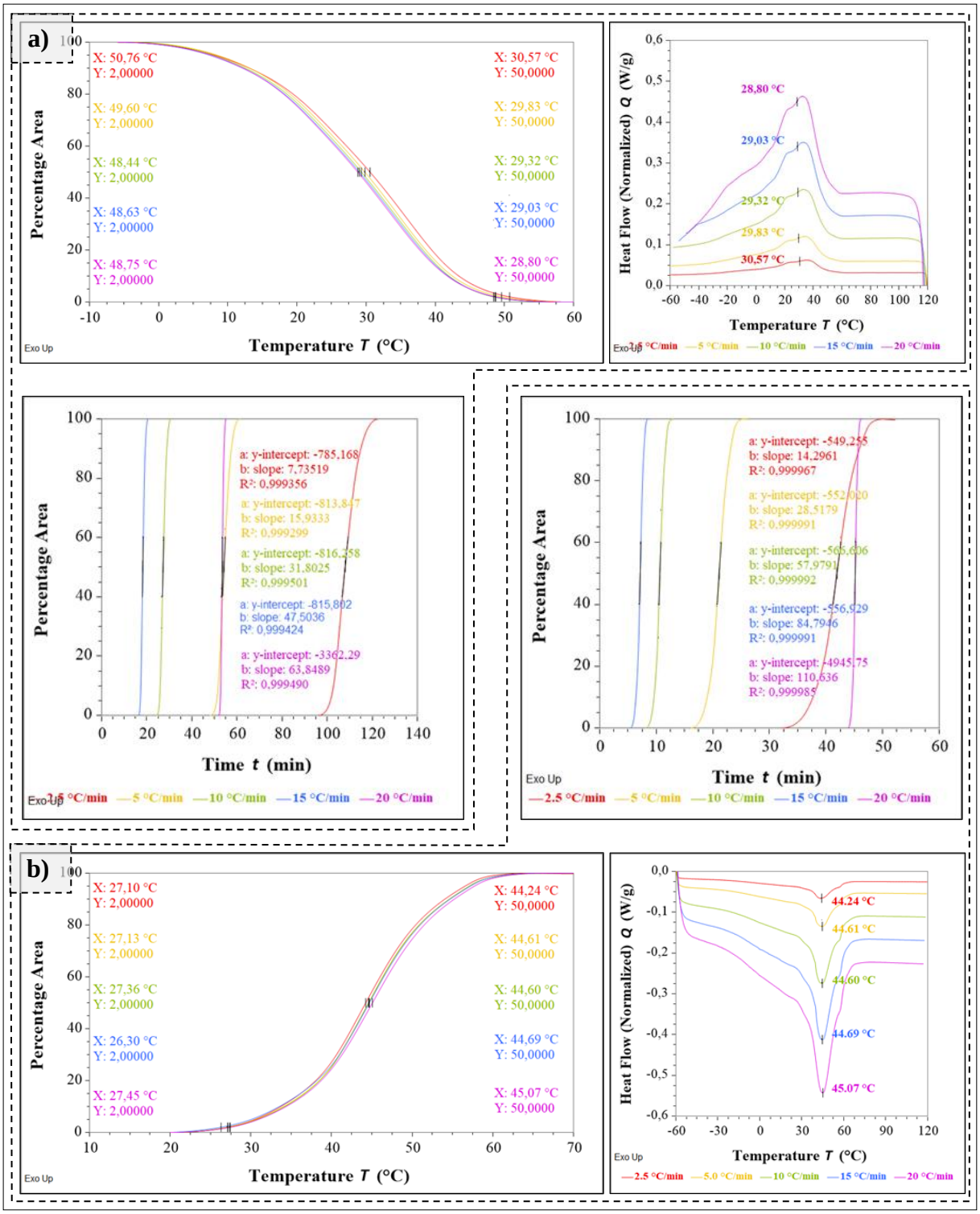

Figure S5.5. Conversion vs. temperature plot, heat flow vs. temperature plot, and conversion vs. time plot for the transition a) from VO_2 (R) to VO_2 (M) and b) from VO_2 (M) to VO_2 (R) for the particles with 2.0 at.% W-doping.